

ROTATION OF HYPERION. II. DYNAMICS

JAMES JAY KLAVETTER^{a)}

Department of Earth, Atmospheric, and Planetary Sciences, Massachusetts Institute of Technology, Cambridge, Massachusetts 02139

Received 4 April 1989; revised 31 May 1989

ABSTRACT

Wisdom, Peale, and Mignard (1984) predicted Hyperion to be in a state of chaotic rotation. Simulations indicate that very precise and well-sampled observations over a few orbit periods are necessary to test this prediction (Peale and Wisdom 1984). I have obtained such a dataset by observing Hyperion for 10 weeks (3.5 orbit periods) at McGraw-Hill Observatory in Arizona using a CCD camera in 1987. Phase-dispersion minimization analysis of the resulting light curve definitively shows that Hyperion is not in any periodic rotation state, thus strongly suggesting it is chaotic (Klavetter 1989). I therefore extended the original dynamical model of Wisdom *et al.* (1984) to include all the modifications necessary to fit the light curve. Numerical simulations indicate the best method used in fitting is (1) choose a well-sampled subset of the light curve to search for and find the area in phase space that approximates the best initial condition, and then (2) fit using some minimization technique to this subset, add the next observation point, and repeat the process for the entire light curve. I conducted such a search and fitting procedure, marginally sampling the necessary phase space. My best fit has residuals comparable with the internal uncertainties of the data. The moment ratios fitted are comparable to those predicted from the *Voyager*-derived shape and are consistent with the satellite having a uniform density distribution.

1. INTRODUCTION

Hyperion (SVII) is unique in the solar system. This satellite of Saturn is the only major body presently rotating chaotically, as demonstrated by this work and Klavetter (1989) (hereafter referred to as Paper I). In Paper I, a well-sampled light curve was presented from observations made at the McGraw-Hill Observatory (MHO) with a CCD photometer. Simple periodic-fitting analysis was done. No regular/periodic rotation state was found that approximated the data. Thus, I attempt to determine Hyperion's rotation state with a model developed from the dynamics outlined in Wisdom *et al.* (1984). The results of these dynamical investigations demonstrate the chaotic nature of Hyperion's rotation and are consistent with Hyperion having a uniform mass distribution.

Table I is a summary of Hyperion's physical characteristics. Note the large axial ratios. No other large satellite has an odd shape. Mimas, for example, is about the same size as Hyperion, yet is well approximated by a nearly spherical ellipsoid. Since Hyperion has such an aspherical shape, it is natural to ask how it could have obtained this shape. It is difficult to determine the relative importance that fragmentation processes and tidal/gravitational forces have had in shaping Hyperion due to a lack of information concerning collisions and material strengths. Smith *et al.* (1982) proposed a model in which collisional fragmentation and reaccretion, perhaps even multiple collisions and reaccretions, account for many of the observed characteristics of the Saturnian satellites. Thomas *et al.* (1983) stated that it was unnecessary to invoke such a "spectacular" explanation for the origins of many of the Saturnian satellites. They noted that cratering statistics indicate that any fragmentation and reaccretion must have occurred at least a few billion years ago based on the crater counts observed. Farinella *et al.* (1983) proposed a model in which Hyperion is the "core" of a disrupted predecessor. Their calculations indicate that the 4:3 orbital resonance with Titan would prevent any reaccretion of secondary fragments, which would either fall into

Titan or would escape from the Saturn system. While the origin of Hyperion is an interesting question, I will deal with the consequences of Hyperion's shape rather than how it was formed.

The *Voyager* spacecraft provided a wealth of new information concerning Hyperion. The *Voyager 2* determination of the shape of Hyperion directly led to the prediction of its chaotic rotation (Wisdom *et al.* 1984). Unfortunately, only about 50% of Hyperion was observed by *Voyager* at high resolution (Thomas and Veverka 1985) so the shape is still uncertain, and it is impossible to map the surface of Hyperion with the topographic features observed. The following results are reported by Thomas and Veverka (1985). Although Hyperion's shape is not precisely ellipsoidal, the best-determined dimensions are $185 \times 140 \times 113 \pm 10$ km. Hyperion's average normal reflectance is 0.21 at $0.47 \mu\text{m}$ and any variations in albedo are essentially averaged out over the disk. Its color is redder than Phoebe but is nearly the same as the dark (leading) side of Iapetus. While there are identifiable craters, the crater density is low compared to other Saturnian satellites. Figure 1 [Plate 59] is one of the highest-resolution images of Hyperion taken by *Voyager 2*. This figure clearly shows Hyperion's highly aspherical shape, which can roughly be described as ellipsoidal from some aspects (see Sec. IV and Fig. 13 for another view). Unfortunately, the *Voyager* spacecraft was not able to determine Hyperion's mass. *Voyager* was not able to independently determine the principal moments of inertia, but these can be calculated if a uniform density is assumed.

The inner satellites of Saturn are mostly ice, as conclusively demonstrated by *Voyager* determination of masses and radii which showed that their densities were of the same order as water ice (Smith *et al.* 1982). Unfortunately, there is no good mass determination of Hyperion. In principle, a mass could be computed from consideration of the 4:3 Titan-Hyperion orbital resonance, but Titan is so much more massive than Hyperion that this is impractical. Cruikshank and Brown (1982) calculated a geometric albedo of $p_0 = 0.28 \pm 0.04$ for a Hyperion with an effective radius of 140 ± 19 km. This is consistent with the value found by Tholen and Zellner (1983) of 0.19–0.25. They give a range of

^{a)} Present address: Astronomy Program, University of Maryland, College Park, MD 20742.

TABLE I. Physical properties of Hyperion.

Property	Value	Reference
radius	$185 \times 140 \times 113 \pm 10$ km	Thomas and Veverka 1985
mass	unknown	
density	unknown	
geometric albedo	0.19 – 0.25	Tholen and Zellner 1983
surface composition	dirty ice	Clark <i>et al.</i> 1984
semimajor axis	24.55 R_s	Woltjer 1928
Distance from Saturn in 1987:		
maximum at elongation	239 arcsec	
minimum at conjunction	86 arcsec	
orbital period	21.277 days	Woltjer 1928
rotational period	chaotic	Wisdom <i>et al.</i> 1984, Klavetter 1989
eccentricity	0.1042 (forced)	Woltjer 1928
inclination	0.43°	Woltjer 1928
V_0	≈ 14.2	(see Table II)
$B - V$	≈ 0.74	(see Table II)
$V - R$	0.41 ± 0.02	Klavetter 1989
J	13.0 ± 0.10	Cruikshank 1979
$J - H$	0.15 ± 0.05	Cruikshank 1979
$J - K$	-0.03 ± 0.07	Cruikshank 1979
$J - L$	>0.55	Cruikshank 1979
lightcurve amplitude	≈ 0.5	Thomas and Veverka 1985

values since they did not know the aspect of the satellite. These values are similar to those found for some asteroids and rocky bodies, but typically less than most icy satellites. Infrared measurements in the region $1.5\text{--}2.6\ \mu\text{m}$ by Cruikshank and Brown (1982) and Clark *et al.* (1984), however, strongly indicate the presence of water ice on Hyperion's surface. It is unknown if water ice is a major constituent of Hyperion's bulk composition or if water ice is just a part of a dirty-frost regolith. Chapman and McKinnon (1986) argued that central peaks would not be found in the largest craters if Hyperion were silicate due to the greater effective strength of cratered rock debris compared to ice. Since they reported finding central peaks in such craters, they believe Hyperion to be an icy satellite. Cruikshank *et al.* (1983) proposed a model in which Phoebe, or some other outer Saturnian body, "hails" dust down to Iapetus and Hyperion. This scenario would not constrain the composition but it could account for Hyperion's relatively low albedo if an icy composition is assumed. Although the colors of the leading (dark) side of Iapetus and Hyperion are similar, Tholen and Zellner (1983) have shown that the broadband colors of Hyperion and Phoebe differ significantly. While this is an interesting area of research, the surface characteristics or bulk composition of Hyperion will not directly affect the dynamics. It will be shown, however, that the principal moments of inertia can be constrained using dynamical considerations. Thus, it is important to consider how different compositional stratifications could affect the moments and the dynamics.

The rotation state of Hyperion can be examined using well-sampled, precise, ground-based observations. Paper I

details the previously published observations that attempted to determine Hyperion's rotation state. All previous datasets are inadequate to resolve Hyperion's rotation state unambiguously because they are undersampled and have large uncertainties due to the background light gradient of Saturn.

Table II lists the previous measurements of Hyperion's photometric properties. There is general agreement among observers, especially since all measurements strongly depend upon the aspect of the satellite which no observer knew at the time of the observations. The mean opposition magnitude of Hyperion is $V_0 \approx 14.3$ with colors of $B - V \approx 0.74$ and $V - R = 0.41 \pm 0.02$ (see Paper I). In addition, Cruikshank (1979) reports the infrared colors listed in Table I. Due to the large light-curve amplitude and the seemingly random nature of chaos, it is possible to unintentionally observe Hyperion preferentially when it is brighter, for example, than its mean opposition magnitude unless it is sampled nearly every night. Another aspect of Hyperion's light curve not known until recently, the opposition surge (Paper I), is exemplified by the observations of Franklin and Cook (1974). They report a mean opposition magnitude significantly brighter than all other observers, but both of their observations were made near opposition, at solar phase angles $\alpha \leq 0.3^\circ$. This is the expected effect of the opposition surge, so these observations, corrected for the phase effect, are consistent with the others. Any discrepancies in the photometric properties listed in Table II may be due, in part, to the nature of Hyperion's rotation state.

In Sec. II, I will discuss the theory necessary to understand the chaos arising from the spin-orbit coupling in the Hyperion-Saturn system. The dynamics covered in Sec. II

TABLE II. Hyperion's photometric properties.

Observer	V ₀ ^a	B - V	β ^b	Δm ^c	N ^d
Harris (1961)	14.16	0.69	----	----	5
Andersson (1974)	14.16	0.78	0.025	0.10	13
Franklin and Cook (1974)	13.93 ^e	----	----	----	2
Degewij <i>et al.</i> (1980)	14.18	0.77	0.380 ^f	0.36	12
Goguen <i>et al.</i> (1983)	14.20	----	0.037	0.48	18
Tholen and Zellner (1983)	14.36	0.73	----	----	2
Conner (1984)	14.82	0.69	----	0.51	8
Klavetter (1985)	14.42	0.77	----	0.45	16
Thomas and Veverka (1985) ^g	----	----	≥0.018	0.52	14
Binzel <i>et al.</i> (1986)	14.42	----	----	1.10	8
Klavetter (1989)	14.23	----	0.056 ^h	0.53	38

a Mean opposition magnitude.
b Linear phase coefficient.
c Lightcurve amplitude.
d Total number of nights observed.
e Both observations at ≤0.3° solar phase angle.
f This is an "adopted value" for all outer solar system objects and not measured for Hyperion.
g Voyager observations.
h Not including opposition surge.

are results from investigations by Wisdom *et al.* (1984) and provide the theoretical framework for this work. Section III outlines the different methods used to analyze Hyperion's rotation state and fully develops the dynamical model used in the fits to my light curve. I will discuss the results and consequences of this research in Sec. IV. The final section lists my conclusions.

II. DYNAMICS

Chaotic motion is deterministic but unpredictable motion due to exponential divergence of nearby initial conditions (Hénon and Heiles 1964; Wisdom 1987). Chaos is not random, it is deterministic. This apparent contradiction will be resolved in this section. I will review the work of Wisdom *et al.* (1984) and discuss the theoretical prediction of Hyperion's chaotic rotation. Various definitions and explanations will be presented which will be used in the analysis and fitting of the light curve (Sec. III).

Until recently, Mercury was the only object in the solar system known to have a commensurate yet nonsynchronous spin rate. Goldreich and Peale (1966) discussed spin-orbit coupling in the solar system and the capture probability of an object evolving into resonance due to tides. They derived a pendulumlike equation for spin-orbit coupling states by averaging nonresonant terms over an orbit period. Wisdom *et al.* (1984) demonstrated that this averaging technique is not applicable when the width of the resonance is comparable to the widths between resonances. The width of a resonance increases with ω_0 where $\omega_0^2 \equiv 3(B - A)/C$ and $A < B < C$ are the principal moments of inertia. ω_0 is a quantity that increases as a uniform body becomes less spherical. Thus, as a uniform body becomes more ellipsoidal, the widths of the resonances get large.

If the widths of the resonances get too large, their separatrixes will begin to overlap. Physically, this means that a body would apparently be in two rotation states at the same

time, such as rotating in the synchronous and the 3:2 state simultaneously. Since it is impossible for a body to be in two resonances at once, chaotic behavior results when this overlap occurs (see Wisdom *et al.* 1984 for a complete discussion and Wisdom 1987 for background material). The approximate point at which this happens is given by the Chirikov resonance overlap criterion (Chirikov 1979). Considering the synchronous and 3:2 states, Wisdom *et al.* (1984) use the Chirikov overlap criterion to show

$$\omega_0^{RO} = 1/(2 + \sqrt{14e}).$$

At the eccentricity of Hyperion, the critical value is $\omega_0^{RO} = 0.31$. Above this value, chaotic behavior will be widespread throughout phase space. For Hyperion, $\omega_0 = 0.89 \pm 0.22$ (Duxbury, as reported by Wisdom *et al.* 1984), much larger than the critical value. Clearly, chaos is expected in an investigation of the rotational phase space of Hyperion.

The phase space of Hyperion can be investigated numerically. To do this, the equations of motion are needed. Following Wisdom *et al.* (1984), an ellipsoid model is used with a, b, c defining a right-hand set of axes fixed in the satellite corresponding to the principal moments of inertia $A < B < C$, as illustrated in Fig. 2. In this case, Euler's equations are

$$\begin{aligned} A \frac{d\omega_a}{dt} - \omega_b \omega_c (B - C) &= -\frac{3}{r^3} \beta \gamma (B - C), \\ B \frac{d\omega_b}{dt} - \omega_c \omega_a (C - A) &= -\frac{3}{r^3} \gamma \alpha (C - A), \\ C \frac{d\omega_c}{dt} - \omega_a \omega_b (A - B) &= -\frac{3}{r^3} \alpha \beta (A - B), \end{aligned} \tag{1}$$

where ω_a , ω_b , and ω_c are the rotational angular velocities about the body axis and r is the Saturn-Hyperion distance. The angles α , β , and γ are the direction cosines with respect to the planet-to-satellite radius vector of the three body axes.

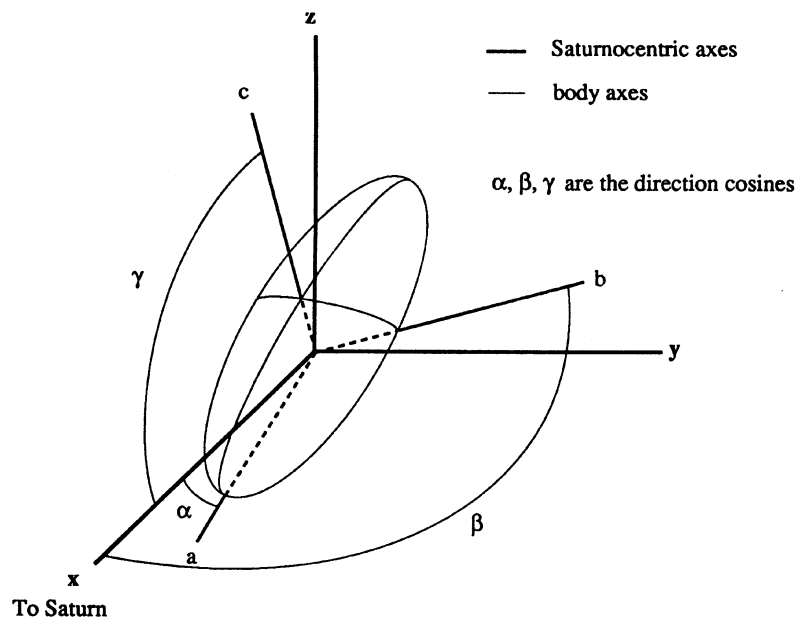


FIG. 2. Definition of the body frame, Saturnocentric (reference) frame at periape, and direction cosines.

Units are chosen such that the semimajor axis is one, the orbital period is 2π , and the dimensionless time is the mean anomaly. All angles are in radians and the corresponding angular velocities are in dimensionless units of rotations per revolution.

Two sets of generalized coordinates are necessary to solve these equations since there will be situations in which a singularity is encountered in any coordinate system and it will be necessary to switch to another coordinate system. One set of coordinates will be the usual Euler angles (Goldstein 1981). The other system will be that chosen by Wisdom *et al.* (1984) and hereafter referred to as the Wisdom coordinates. Both coordinate systems have a reference frame defined at periape as follows: the x axis is parallel to the planet-to-satellite vector, the y axis is parallel to the orbital velocity, and the z axis is normal to the orbit plane, completing a right-hand coordinate system. (See Fig. 2.) The three rotations defining the Euler angles, as illustrated in Fig. 3, are defined by the following rotations. First, the body axes are rotated

about the z axis by an angle θ . Next is a rotation about the new x axis, the x' axis in Fig. 3, by an angle φ . The third rotation is about the new z axis, the c axis, by an angle ψ . The transformation from the Saturnocentric axes to the body axes using the Euler angles is derived in Appendix A. The Wisdom coordinate system differs in the third rotation ψ^w , which is about the new y axis. In either coordinate system, the rotations θ , φ , and ψ describe the spatial orientation of the ellipsoid.

I will derive the equations of motion for the Euler coordinates. Wisdom *et al.* (1984) outline the derivation of the equations of motion for the Wisdom coordinates. The components of the angular velocities about the body axes in Euler coordinates are

$$\begin{aligned}\omega_a &= \dot{\theta} \sin \varphi \sin \psi + \dot{\varphi} \cos \psi, \\ \omega_b &= \dot{\theta} \sin \varphi \cos \psi - \dot{\varphi} \sin \psi, \\ \omega_c &= \dot{\theta} \cos \varphi + \dot{\psi}\end{aligned}\quad (2)$$

as derived in Appendix B.

The direction cosines are

$$\begin{aligned}\alpha &= \cos \theta \cos \psi - \sin \theta \cos \varphi \sin \psi, \\ \beta &= -\cos \theta \sin \psi - \sin \theta \cos \varphi \cos \psi, \\ \gamma &= \sin \theta \sin \varphi,\end{aligned}\quad (3)$$

as derived in Appendix C. The equations of motion are derived by differentiating Eq. (2) with respect to time and substituting Eqs. (1) and (3) into the new second-order equations. These are then the equations of motion. The details of the derivation are given in Appendix D. The variables used in the equations of motion, θ , φ , ψ , $\dot{\theta}$, $\dot{\varphi}$, $\dot{\psi}$, and $\dot{\psi}^w$ are the *dynamical state variables*. These state variables, as well as two parameters related to the principal moments of inertia (see Sec. III), define a *rotation state*. If the rotation state is specified at a certain time, such as the true anomaly, it is known as an *initial condition*.

It has already been demonstrated using the Chirikov over-

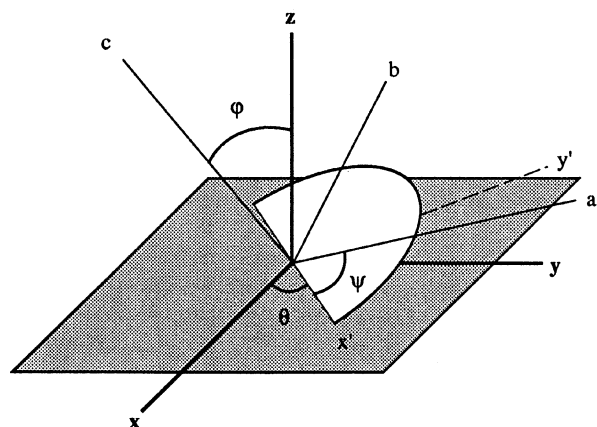


FIG. 3. Rotations defining the Euler angles. The axes are labeled as in Fig. 2.

lap criterion that the phase space of Hyperion's spin-orbit coupling will exhibit large scale chaos. As posed, however, the phase space is six dimensional and difficult to visualize (in this paper, *phase space* is the number of dimensions under investigation). If the spin axis is fixed perpendicular to the orbital plane, as would be expected for a tidally evolved synchronously rotating satellite, and the corresponding angular velocity $\dot{\theta}$ is the only nonzero component of the velocity vector, the phase space is reduced to two dimensions with explicit time dependence. This is the case in which the spin axis of the satellite is constrained to be perpendicular to the orbit plane. With these constraints, Goldreich and Peale (1966) derive the equation of motion for θ without external torques as

$$\ddot{\theta} + (\omega_0^2/2r^3)\sin 2(\theta - f) = 0.$$

where f is the true anomaly of the satellite. This is just a special case of the full three-dimensional problem, however, with $\varphi = \dot{\varphi} = \psi = \dot{\psi} = 0$. The problem is now reduced to one that can be easily visualized by a Poincaré plot, or surface of section, in which the angular velocity is plotted versus the orientation at every periapse passage. Wisdom *et al.* (1984) demonstrate the onset and growth of chaos as ω_0 increases. When ω_0 is as large as Hyperion's value, chaos is a major feature of phase space. Figure 4 is the surface of section appropriate for Hyperion. In a surface of section, quasiperiodic zones are identified by the individual points that lie on a well-defined curve. The apparently random assemblages of points are the chaotic regions.

During Hyperion's tidal evolution, the satellite is driven towards the synchronous state and inevitably ends up in the

large chaotic zone seen in Fig. 4. Wisdom *et al.* (1984) demonstrate that Hyperion is attitude unstable for the synchronous state and the 1:2 rotation state. That is, infinitesimal deviations of the orbital axis from the perpendicular to the orbital plane will cause further deviations that grow until the satellite starts to tumble. Only the small 9:4 and 2:1 rotation states are attitude stable. Thus, there is virtually no possibility of Hyperion entering the synchronous or 1:2 state since the chaotic zone is also attitude unstable. Capture into any other state is extremely unlikely since Hyperion must enter the state with the spin axis "randomly" oriented perpendicular to the orbital plane and must also stay in the special configuration long enough for the weak tidal dissipation to capture the satellite into the stable rotation state. Numerical simulations support this expectation (Wisdom *et al.* 1984).

The above analysis was of a restricted model in which the spin axis was set perpendicular to the orbital plane. The evidence has clearly demonstrated Hyperion's chaotic nature, but the full equations of motion have not yet been fully explored. Fortunately, these equations can be used to predict the nature of Hyperion's rotation state using Lyapunov characteristic exponents. Lyapunov exponents measure the average rate of exponential separation of nearby trajectories (see Wisdom 1983 for a more complete discussion). A nonzero Lyapunov exponent indicates the reference trajectory is chaotic while zero exponents indicate quasiperiodic motion. Wisdom *et al.* (1984) calculate Lyapunov exponents for a number of trajectories and find them to be nonzero, indicating chaotic behavior for the Hyperion system. The Lyapunov exponents can also be a measure of the timescale for diverging initial conditions. The values found for the Hype-

Hyperion Surface of Section

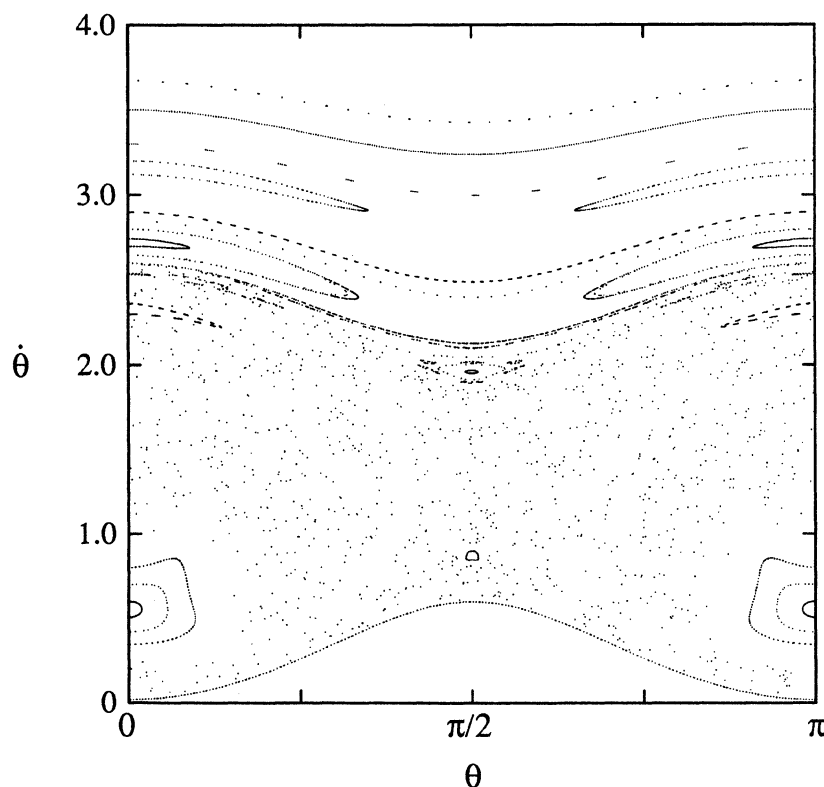


FIG. 4. Surface of section for Hyperion. The equations of motion are integrated and the orientation versus spin rate is plotted at each periapse passage. Quasiperiodic areas are surrounded by points that form a nearly continuous curve. Chaotic areas are the seemingly random scatter of points. Fifteen initial conditions were integrated for 300 points each to produce this plot. The synchronous, 1:2, and 2:1 rotation states, are completely surrounded by the large chaotic zone. The 3:2 state is non-existent.

tion system indicate that initially close rotation states widely diverge in only two orbital periods.

One important aspect of chaotic motion often ignored by previous observers of Hyperion is the constraint of gathering data on a chaotic system. Wisdom *et al.* (1984) point out that meaningful results will not be obtained if the period of the observed object varies on a timescale that is short compared to the time between the observations. If an object is rotating chaotically, techniques in which the data are folded back cannot be used to obtain meaningful results. Quasiperiodic solutions are not only possible, but common with undersampled data that is folded back and subjected to least squares analysis (Peale and Wisdom 1984). Thus, the 13.1 day period derived from *Voyager* data (Thomas *et al.* 1984; Thomas and Veverka 1985) does not imply any regular rotation period since the data are undersampled (see Paper I). Only with a sampling rate of about one observation per 1.5 days will be ambiguities be resolvable (Peale 1986; Peale and Wisdom 1984).

III. ANALYSIS

The observations and data reduction techniques have been published in Paper I (Klavetter 1989). Figure 5 is the raw Hyperion light curve, reproduced from Paper I (Fig. 2 of that paper). Note the opposition surge (or spike) near periape. Refer to Paper I for details of the data acquisition and reduction.

Analysis of my observations will be carried out on two independent levels: period determination and dynamical fitting. First, I will review the period-determination analysis for timescales ranging from hours to months. It has been demonstrated that there is no plausible period that can describe the light curve, even considering the observational and phase-fitting uncertainties (Paper I). Because of this lack of a coherent period in the light curve and the theoretical expectation that Hyperion is chaotically tumbling, a second analysis will be carried out based on the dynamical model derived in Sec. II. It is important to note that any

conclusion inferred from the period determination is independent of the dynamical fitting.

In subsec. a, I will review the period determination techniques used to examine any regularities in Hyperion's light curve. In the next subsection, I will derive various modifications to the model presented in Sec. II such that chaotic rotation can be modeled and fit to my light curve. In doing so, four parameters in addition to the state variables will be determined from the analysis: the mean opposition magnitude, the phase coefficient or slope parameter, and two of the principal moments of inertia normalized to the third. In subsec. c, a general method of determining the initial condition of a light curve is presented. In subsec. d, I will present results of fits to the MHO light curve based on a fraction of phase space searched.

a) Period Determination

The Hyperion light curve was analyzed with a phase-dispersion minimization (PDM) algorithm. This technique yields an unbiased best period with no dependence on a fitting function (Stellingwerf 1978). With PDM analysis a range of periods are assumed, and the light curve is folded back upon itself. For each period in the range, the data are then sorted in a manner such that there are at least a few data points in each bin. The dispersion about the mean value is calculated for each bin and the total dispersion is calculated for the periods tested. This allows the best period for any given dataset to be determined by finding the minimum in the plot of period versus dispersion. When the dispersion is small, the brightness at any given phase is approximately the same and the data are well described by that period. PDM analysis does not use a fitting function, so there is no prior assumption about the type of periodicity that is detected by inspection of the PDM plot.

The PDM plots of the MHO light curve agree to within a few percent for three methods of phase correction: (1) the *H* and *G* phase correction (Bowell *et al.* 1987), (2) linear phase correction with some or all of the observations, and (3) no phase correction. With PDM analysis, the best period found for the mean opposition magnitude light curve of the nightly means is 6.6 days (see Paper I). The statistical significance of this period can be measured by comparing the uncertainties of the data with the variances of each bin. For any given period, the mean over all bins of the square root of the variance should be comparable to the uncertainties in the data for an acceptable fit. This quantity for the 6.6 day period is 0.11 mag, a factor of 5–10 larger than a typical observational uncertainty of 0.01–0.02 mag. Another measure of the significance of the fit is demonstrated by inspection of the phase plot (Fig. 4 of Paper I) in which the data are folded back using the 6.6 day period. There are large differences at various phases, indicating the fit is not good. See Paper I for complete details of this analysis.

The period for the best fit is similar to those periods found from numerical simulations of a chaotically rotating Hyperion-modeled ellipsoid using traditional least-squares analysis (Peale 1986; Wisdom and Peale 1984). Indeed, Peale and Wisdom (1984) found that it was easy to define intervals of numerically generated light curves that yielded desired periods. Although PDM analysis may be used to determine the best period over a given time interval, this period may not have physical meaning for the system under consideration. The statistical comparison above and the rotational phase

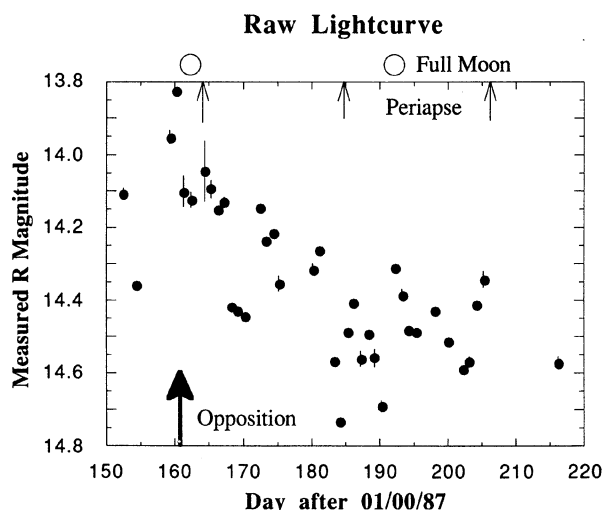


FIG. 5. Raw Hyperion light curve. Measured Johnson *R* magnitudes uncorrected for mean opposition distance or solar phase angle versus time in days after 01/00/87. Error bars are not shown for points having an uncertainty less than 0.01 mag (the size of the dot).

plot (Paper I) demonstrate that the best period chosen through PDM analysis is not a good fit.

Similarly, a best period was calculated using the entire dataset instead of the nightly means. Periods from 2 hr to 5 days sampled every hour were tested with the entire dataset. The dispersion is again a factor of 10 larger than that expected from the observational uncertainty, indicating that none of these fits are adequate to describe the light curve. Rotational phase plots of the best periods from the PDM plot confirm that none of the fitted periods are adequate. This demonstrates that short periods are not fit by the data, consistent with the observational result that no measurable trends were seen in any of the nightly variations.

Various phase functions for both the nightly means and the entire dataset were analyzed using the PDM technique. All phase plots for absolute and local minima and corresponding harmonics were plotted and found to be as scattered as the rotational phase plot shown in Paper I. No well-defined period was found for any of the minima. No period from 1 hr to 30 days fits the dataset satisfactorily.

b) Application of the Dynamical Model

The results of PDM analysis show that there is no well-defined periodic variation in the light curve obtained from my observations taken at MHO. This is consistent with a chaotic rotation state as predicted by Wisdom *et al.* (1984). Since the uncertainties are small and the sampling is on the order of one observation per day, it is not reasonable to conclude that Hyperion is in a regular, undetected, rotation state. There will be further discussion of this in the next section. Now I will attempt to fit the model based on the dynamics as developed in Sec. II to the light curve presented in Paper I (shown in Fig. 5). Some modifications need to be made, however, to convert the rotation state as defined by the equations of motion to the light curve as seen from Earth.

The data were first corrected for light travel time. What is observed on Earth is the position 70 or more minutes prior to the time of the observation at the distance of Hyperion. To determine these light travel times for each observation, I interpolated the values given in the 1987 *Astronomical Almanac*. Although Hyperion's brightness does not change significantly on such timescales, chaotic motion is extremely sensitive to the initial condition. A difference of 70 min in the time of observation at the beginning of the light curve can propagate to a hundredth of a magnitude or more difference at the end of my light curve. This is of the same order as a typical uncertainty in my light curve.

In order to compare my light curve with the model, the position of Hyperion in its orbit must be determined. I used the general formulas from the *Explanatory Supplement to the Astronomical Ephemeris and the American Ephemeris and Nautical Almanac* to calculate the mean anomaly, the eccentricity, and the other orbital elements. Solving Kepler's equation gives the eccentric anomaly which can, in turn, be transformed to the true anomaly. The details of the procedure are given in Appendix E. The true anomaly is the state variable used as the time variable in the dynamical model.

The dynamical model, as it has been developed in Sec. II, allows the rotation state to be calculated given an initial rotation state. In the case of Hyperion, the rotation state consists of the three angles necessary to specify its orientation in space, the three angular velocities defined in Eq. (2), the three principal moments of inertia, and a time variable such

as the true anomaly. In general, the principal moment of inertia for a homogeneous ellipsoid is given by the equation

$$A = [(b^2 + c^2)/5]m,$$

where A is one of the principal moments of inertia, b and c are the semiaxes, and m is the mass. The equation is cyclic for B and C . Because there is no adequate mass determination of Hyperion, the moments cannot be computed. Following the procedure outlined by Wisdom *et al.* (1984), I normalized the principal moments by the largest, C . Thus, whenever referring to the principal moments of inertia, it will imply the ratios A/C , B/C , and the redundant C/C . Note that the equations of motion are still completely general and independent of the actual value of C because the Euler equations are linear in the moments. Although the absolute values of the mass and moments are not known, the dynamics can be computed using this formalism.

Determination of the rotation state does not allow direct comparison with the light curve. Integration of the initial condition produces a set of dynamical state variables from which the cross sectional area of the model ellipsoid and relative magnitude can be calculated. The relative magnitude of a uniform ellipsoid depends upon the orientation of the ellipsoid relative to Earth, independent of the velocity state variables. The equation of an ellipsoid is

$$1 = \frac{x'^2}{a^2} + \frac{y'^2}{b^2} + \frac{z'^2}{c^2},$$

where the primed coordinates represent the body frame and $a > b > c$ are the principal semiaxes. A set of three rotations can be applied to the body axes to find the equation of the Hyperion ellipsoid in the Saturnocentric coordinate system. These are the Euler (Wisdom) rotations defined in Sec. II. The matrix that converts the body coordinates to the Saturnocentric coordinates, A , is calculated in Appendix A. $\mathbf{x} = A\mathbf{x}'$ is used to calculate the equation of the ellipsoid in the unprimed, Saturnocentric, coordinate system. The projected area of the ellipse is found by substituting the equations for the body axes into the equation of the ellipsoid and differentiating with respect to x to give the projection on the y - z plane. The equations of the ellipsoid's projected area expressed in the dynamical state variables are derived in Appendix F.

The projected area of the Hyperion ellipsoid can now be calculated in the Saturnocentric coordinate system. Because the observations were made from Earth, however, a transformation of the Saturnocentric coordinate system to a geocentric coordinate system must be made. The e coordinate system is an Earth-based system defined as follows: the e_1 axis is parallel to the Earth-to-Saturn (or Hyperion) vector, the e_3 axis is perpendicular to the plane of the ecliptic, and the e_2 axis completes a right-hand coordinate system. The transformation to the geocentric axes involves two rotations. The first rotation, as shown in Fig. 6(a), is by an angle, ξ , about the z axis. This rotation aligns the x axis with the e_1 axis. The angle ξ is the projection of $\hat{x} \cdot \hat{e}_1$ onto the ecliptic. ξ changed by less than 0.7° during this time, so there is negligible error introduced in the projected area by assuming ξ is constant.

The second rotation necessary to transform the Saturnocentric coordinate system to a geocentric one is an angle B about the new y axis to orient Hyperion's orbital plane to the plane of the ecliptic, as shown in Fig. 6(b). I used the values of B as tabulated in the *Astronomical Almanac*, interpolated to the appropriate time. The orbital inclination of Hyperion

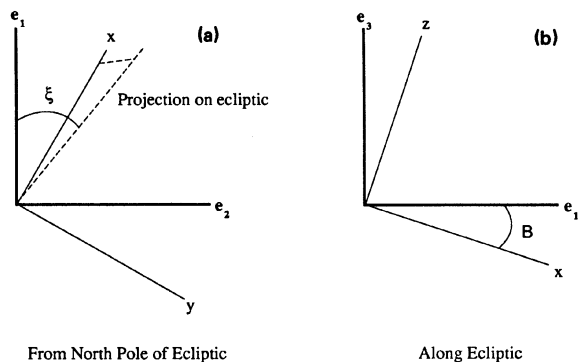


FIG. 6. Two rotations necessary to bring the Saturnocentric frame in line with the geocentric frame. These are necessary to find the projected area of Hyperion as seen from Earth. The first rotation is about the Saturnocentric z axis by an angle ξ . This is a projection of the angle between the Earth-Saturn line and the line of Hyperion's periape, analogous to a right ascension of Hyperion as seen from Earth. The second rotation is about the new y axis by an angle B , analogous to the declination of Hyperion as seen from Earth.

to the plane of the rings, which is the reference plane for the tabulation of B , is 0.4° . Thus, the effect of Hyperion's inclination to the calculation of the projected area is negligible and has been ignored.

The rotations ξ and B are analogous to a right ascension and declination of Hyperion as viewed from Earth. They differ slightly from right ascension and declination in that ξ has a different zero point than right ascension and B corrects for the inclination of Saturn to the ecliptic. These two rotations, in addition to the above transformation from body axes to Saturnocentric axes, are adequate to transform the rotation state to a projected area as seen from Earth. Appendix F gives the full details of the procedure used to calculate the projected area of Hyperion as seen from Earth from the dynamical state variables.

In order to relate the rotation state of Hyperion to my light curve, the projected area must be converted to a magnitude. Assuming albedo remains constant for any aspect of the satellite, the relative magnitude is $m = -2.5 \log A$, where A is the projected area normalized to the maximum projected area. There is a constant offset between this magnitude and the magnitudes obtained from my light curve. This number is related to the mean opposition and will be one of the parameters used in the fitting process.

The Duxbury values of the principal semiaxes, as reported by Wisdom *et al.* (1984) were used to compute the projected area of the Hyperion modeled ellipsoid. The best-fit ellipsoid found has principal semiaxes of $190 \times 145 \times 114 \pm 15$ km. This is consistent with the value by Thomas and Veverka (1985). The differences in the two determinations of size are less than 3% in each dimension, much less than the formal uncertainties. An inspection of Fig. 1, one of the highest-resolution *Voyager* images, shows that Hyperion can have a projection well fit by an ellipse, consistent with Hyperion's shape being closely approximated by an ellipsoid. Other images, though, do not indicate such a regular ellipsoid (see next section and Fig. 13). The effect of uncertainties in Hyperion's shape and albedo will be discussed in the next section.

Integration of the equations of motion for the ellipsoid model, as given in the previous section and Appendix D,

were performed using the Bulirsch-Stoer method of numerical integration (see Press *et al.* 1986). During the course of an integration, it was necessary to switch coordinate systems to avoid singularities. The mathematical details of the coordinate conversions are derived in Appendix G.

c) Numerical Simulations

The model presented is of an ellipsoid in the Hyperion-Saturn system. An initial condition integrated over time gives the rotation state, and therefore relative magnitude of the system, at any other time within the precision of the computer. The difficulty is finding the initial condition corresponding to my light curve. Numerical simulations indicate that phase space becomes more complex as longer intervals of observations are examined. Figure 7 illustrates this increase in complexity. This plot was obtained by numerically calculating a light curve with the same sampling intervals as my MHO light curve using a random initial condition chosen to mimic the features seen in that data. I then calculated the sum of the squared residuals χ^2 normalized to the number of observations for a range of values along the principal axes for both the entire light curve and a subset of well-sampled points, keeping the other dynamical variables constant at their chosen values. The two curves shown in Fig. 7 are calculated for the velocity variable along one of the principal axes. Note that the solid-line curve associated with the entire light curve displays more peaks and valleys than the dashed line corresponding to the light-curve subset. The line for the entire light curve is also much narrower near the value of the known initial condition than the subset, although both exhibit approximately the same value at zero displacement. Thus, a fitting routine would have difficulty finding the absolute minima for the entire light curve because of the presence of so many local minima. The same

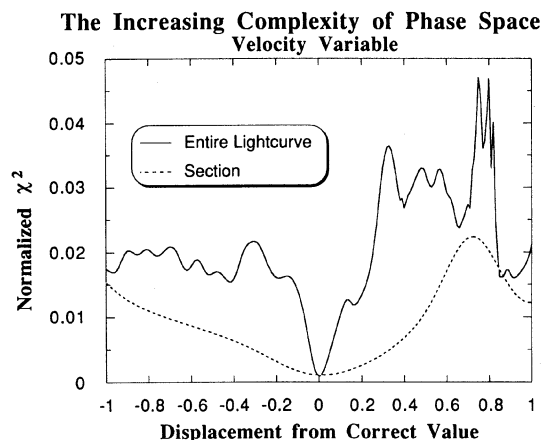


FIG. 7. Illustration of how the complexity of phase space increases with the number of observations. All dynamical variables were set equal to their known values except for one component of the velocity which varied between plus and minus one rotation per revolution from its correct value. This is plotted along the abscissa. Plotted along the ordinate is the χ^2 per number of points for two datasets. The solid line corresponds to a numerically generated light curve at the same sampling rate as the MHO light curve (Fig. 5), the dashed line to a well-sampled subset of that light curve, 12 observations in a 13 day interval.

fitting routine would not encounter this difficulty for the curve corresponding to the subset.

These results are very general. The same features seen in Fig. 7 appear for other initial conditions. Similar curves are calculated for the other velocity components, although the effect is less extreme for the other state variables (see below). The subset chosen corresponds to 12 points out of a 13 day sampling interval from the MHO data. The behavior is similar for other well-sampled subsets. A Gaussian error distribution of 0.03 mag per observation was added to this numerically generated light curve to better simulate a realistic χ^2 distribution. All but one dynamical state variable was kept constant as that one was varied. This is essentially a one-dimensional version of the problem. However, this behavior was seen for the other velocity variables and for different initial conditions. Therefore, a generalized fitting routine would have more success fitting fewer well-sampled observations than fitting the entire light curve, although this is perhaps somewhat counterintuitive.

A general procedure for determining initial conditions for a Hyperion light curve can be outlined. The strategy is to choose a well-sampled portion of the light curve as the dataset and search all of phase space using the ellipsoid model developed above (remembering that phase space is defined as the number of dimensions or parameters). The sampling rate, or grid spacing, is discussed below. Once an approximate rotation state is found that matches the dataset, the rest of the observations are added singly and fitted to converge on the initial condition. Numerical simulations (Klavetter 1985, unpublished) demonstrate that when using this technique, there is an exponential decrease in the uncertainty of the initial condition as the number of observations increase. This can be seen in Fig. 8, in which the log of the residuals of the moment variables are plotted versus observation number for a light curve with known moment ratios. For this plot, data with 0.03 mag simulated observational error was fit using the above algorithm and the residuals at each step were plotted. There is a dramatic decrease in the residuals, almost down to machine precision in the 60 day interval. Wisdom (1987) and Chakrabarty (1988, unpublished) found a similar exponential decrease in the uncertainty of the initial conditions with increasing number of observations for a simple chaotic system.

Phase space for the Hyperion system consists of ten di-

Decrease of Uncertainty with increasing Observations

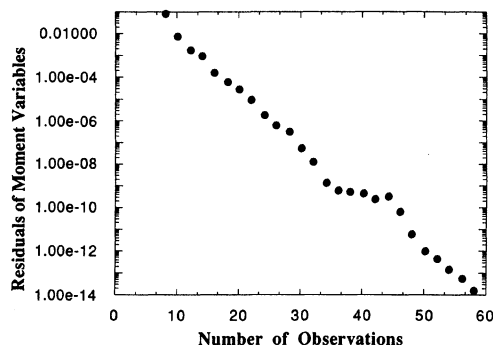


FIG. 8. There is a dramatic decrease in the uncertainty of initial conditions as exemplified by the decrease in the residuals of the moment variables for this Hyperion test system.

mensions: the three spatial angles, the three angular velocities, the two principal moments of inertia ratios, the phase slope parameter, G , and the mean opposition magnitude, H . How finely the phase space needs to be searched to find a "close" initial condition is a difficult problem because of the inherent complexity of the phase space. To estimate the necessary sampling, an initial condition is chosen and one dimension of phase space is varied while the other dimensions are held constant at their known values, as in Fig. 7. The resulting light curves can then be examined to determine the sampling interval.

In Fig. 7, for example, if all of the other state variables were known exactly, the necessary sampling would be once every 0.7 (dimensionless) rotations per orbit, the approximate turnover point of the subset (dashed) curve. Any minimization technique sampled at a rate greater than this would not necessarily be able to converge to the true answer. This should be contrasted with sampling of less than 0.1 if the entire light curve were used. Since there are eight state variables to vary, this corresponds to a savings of a factor of approximately $7^8 \approx 10^6$ integrations. Since this is a simplified one-dimensional analog of the multidimensional task, a sampling interval less than 0.7 will be used for the fitting (see next subsection).

The above procedure was performed using one of the angular state variables instead of a velocity variable to estimate the sampling interval necessary for the angular state variables. In this case, the turnover point was at a displacement of approximately 1.0 (dimensionless) radians. This is shown in Fig. 9, a plot similar to Fig. 7, but using an angular state variable to be varied instead of one of the velocity variables.

Figure 10 is the corresponding plot for one of the moment ratio variables. The curve is very shallow but is well behaved and indicates that when searching phase space using a subset of the light curve, the best initial conditions found are not sensitively dependent on the value of the moment ratios. This was indeed found to be the case (see next subsection).

In addition to the dynamical variables and moment ratios,

Determination of Grid Spacing
Angle Variable

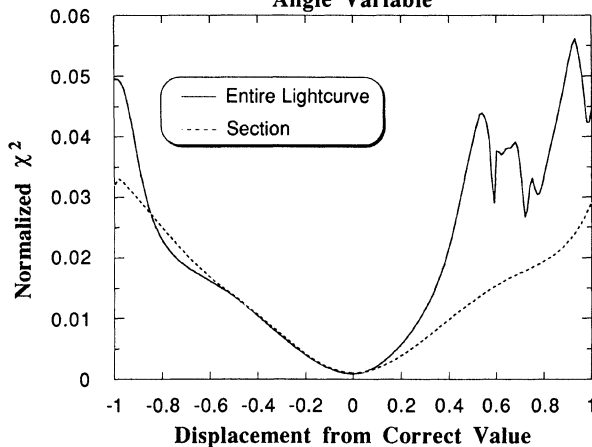


FIG. 9. Plot similar to Fig. 7, but one of the angular variables were varied while the other state variables are held constant. The ordinate is the same as in Fig. 7 and the abscissa is in radians. The subset just starts to turn up at a little less than -1 radian. This is an indication of the grid spacing necessary to sample phase space.

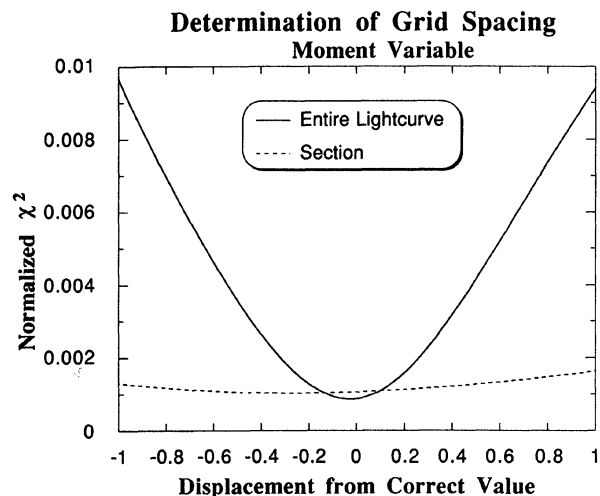


FIG. 10. Plot similar to Fig. 7, but one of the moment ratio variables were varied while the other state variables are held constant. Note that the value of the moment ratio is insensitive to the variations using the light curve subset but becomes very important for the entire light curve.

there are two observational parameters, H and G , which need to be considered when fitting an observed light curve. This is because precise values for H and G are not available from the data due to the unknown varying aspect of Hyperion, as discussed in Paper I.

The total number of initial conditions necessary to search all of phase space effectively is calculated by dividing the range of each variable by the grid spacing necessary for that variable. For example, to search the entire range of the angular state variables of 0 to π at a sampling interval of 0.5 radians would require six integrations. Since there are three angular state variables, there will be a total of $6^3 \approx 100$ integrations for just the angle variables. Similar considerations apply to the velocity, moment, and H and G variables.

An exhaustive search in which every grid point is integrated over the entire light curve, or even a subset of the light curve, may not be necessary. If using a subset of the light curve in which the first point is a maximum or minimum, after correction for phase effects, one or two of the angle variables are constrained to be specific values, thus reducing the number of grid points necessary to search. To be valid, this technique requires the observation to be a global extremum in which the projected area of the satellite measured is a minimum or a maximum. The minimum or maximum of the light curve is not guaranteed to correspond to the maximum or minimum projected area of Hyperion, however, unless the time interval of the observations is large enough to have sampled the satellite from all aspect angles.

In general, the initial condition can be constrained without integrating the equations of motion by comparing the calculated mean opposition magnitude with that measured. If the first magnitude calculated from the projected area is not consistent with the mean opposition magnitude, calculated to be $H = 13.81 \pm 0.05$ (see Paper I), that initial condition is rejected. Most initial conditions can be discarded without any integration of the equations of motion using this comparison. This technique for filtering the grid of initial conditions to be searched is dependent on the first observation and mean opposition magnitude being accurate. To

compensate for possible error, one can (1) assign a large uncertainty to the datum, and/or (2) perform the search using a number of different subsets.

Even if the first observation is fit by the initial condition, it is possible to prematurely end the integration if it becomes obvious the initial condition is not going to fit the light curve. This is done by integrating the initial condition to the time of the second observation in the light-curve subset and comparing the model and observed magnitudes. If they agree to within the uncertainty of the observation and of the mean opposition magnitude, the integration is continued, otherwise the integration is terminated and the next initial condition is checked. To allow for error, this technique requires a large uncertainty to be assigned to each point, and/or searching a number of different subsets of the light curve.

With this sort of filtering, a μ VAX can check an average of 320 initial conditions per minute. Thus, searches of thousands of initial conditions can be done in minutes whereas searches of tens of millions of initial conditions can take weeks of computer time. Fortunately, I had weeks of computer time available to search phase space and fit the model to my MHO data.

d) Model Fitting to the MHO Data

I performed a search of the above type using six μ VAXes over a time interval of 3–5 weeks. I used four different subsets, two of them using slightly different offsets in their searches. In this amount of time, I was able to complete thorough, but not exhaustive, searches of the appropriate areas of phase space. This subsection describes those searches and shows the results.

I searched four subsets of the MHO light curve with grid spacings of 0.5 radians for the angular state variables, 0.4 for the velocity state variables, and 0.3 for the moment ratios. Except for the moment variables, these values are approximately half the value found from inspection of Figs. 7, 9, and 10. There is a trade off between the grid spacing and the amount of computer time, and these values were small enough to adequately search phase space but not so small as to be prohibitively costly in terms of computer time. I searched the entire range of the angular variables from 0 to π . The range searched for the velocity variables was from -3 to 3 , discarding all initial conditions in which the sum of the velocity components was greater than the absolute value of three. Velocities outside this range were not considered because they produced light curves in which the variation over a typical night was larger than seen in the data (see Paper I). The range of the moment ratios searched was 0.6 centered on the Duxbury-derived values of $A/C = 0.60$ and $B/C = 0.86$ (as reported by Wisdom *et al.* 1984). The range of G searched was 0 to 0.20 at a sampling of 0.05 , based on the range of plausible G parameter values. The H parameter was calculated from the projected area of the first model point and only those variables which produced a reasonable H were continued. Thus, H was used as a filter as described above. This corresponds to approximately 10 million integrations which can be finished in weeks on a μ VAX computer. I assigned a 3σ range on the uncertainty of all observation magnitudes and the mean opposition magnitude, H , to allow for error in the observations, shape, and albedo. The programs ran for a total of 2–5 weeks on each μ VAX and wrote the initial conditions which fit greater than eight points to a file. The results of these searches produced initial conditions that typically clumped around a few values.

The initial condition was determined more accurately using the downhill simplex method (see Press *et al.* 1986). This algorithm provides a robust method of finding a minimum in a complex phase space. The simplex method does not use derivatives to find a gradient in phase space, but computes a starting simplex of $N + 1$ dimensions, where N is the number of dimensions searched. The vertices of this simplex are the function to be minimized evaluated at the values supplied as a starting guess. Various geometrical transformations are applied to the vertices of this simplex, such as expanding, contracting, and reflecting, to find the minimum in phase space. The simplex performs these transformations until all the vertices have converged.

The clumps of initial conditions found from the phase-space search were input for the simplex. These clumps typically had the most variation in the moment ratios indicating that I did indeed oversample these state variables. The ambiguity was resolved in the fitting, however, since the light curve becomes increasingly sensitive to the moment ratios as the number of observations increase, as can be seen in Fig. 10. In all cases, the minimum found with the simplex fitting technique proved to have a significantly smaller χ^2 than the second best clump of initial conditions found from the search, usually by a factor of 2 or greater. This was shown by choosing the factor that governs the magnitude of the simplex's geometrical transformation to be small and refitting without the initial condition first found. After the initial simplex fit, another observation point was added to the subset of my light curve under investigation and the fitting was done on this new subset with the simplex algorithm. This procedure was continued until the entire light curve was fit, as described in the previous subsection.

Two observations were not included in this fit. One was the observation on day 160 at extremely small solar phase angle $\alpha = 0.03^\circ$. The phase function used may not fit the opposition surge well, as described in Paper I. The other observation omitted from the fit was the one on day 164. It has a formal uncertainty of almost 0.1 mag, too large to be meaningful for the fits.

Except for the observation point on day 164 above, the formal uncertainties were typically of the order 0.01 mag. I assigned a minimum observational uncertainty of 0.01 mag to those observations that had a formal uncertainty smaller than this. At various times in the fitting process, I used the statistical $1/\sigma_i^2$ weighting function and refit. The differences between these and the unweighted fits were negligible for most of the trials. There was virtually no difference between weighted and unweighted fits as the number of observations approached the maximum number, indicating that statistical weighting is unimportant.

Four different subsets, two of them searched twice with different regions of phase spaces, were originally used as datasets to be searched. Two of them differed only in one observation point and these were merged immediately after the initial search. Two others were terminated during the simplex fitting stage since the first became very poor in comparison with the other trials as judged from visual inspection of the intermediate light curves and comparison of the χ^2 . The other three were continued until all points had been added and fit in the manner described above. Of these, two of them had a χ^2 about 50% larger than the best fit. Visual inspection of the resulting light-curve fit confirms that these were much worse than the best one found.

Figure 11 is a plot of the light curve, uncorrected for phase

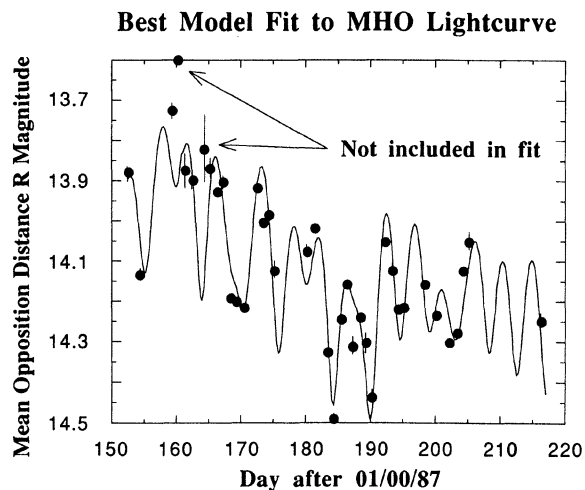


FIG. 11. Best model fit to MHO light curve. The points are the measured R magnitudes corrected to mean opposition distance but uncorrected for phase. The solid line is the best model fit obtained with the method described in the text.

effects, with the best-fit model superposed. Table III lists the initial condition used to produce this light curve. The uncertainties in the initial condition were calculated from the covariance matrix of a nonlinear least-squares fit to the entire light curve (see next section). Note that the values of the state variables are in Wisdom coordinates. The numerical value of the first six state variables are, therefore, somewhat arbitrary because these variables would have different values if expressed in Euler coordinates, yet the light curve would be the same. The significance of this fit will be discussed in the next section.

Figure 12 is the second best fit plotted as in Fig. 11. Table III lists the initial conditions for this model fit. As can be seen by inspection of Figs. 11 and 12 or a comparison of χ^2 from Table III, this fit is significantly worse than the best fit. The second best fit is very far away in phase space as can be seen from Table III. The initial conditions were far enough from each other and phase space is complex enough that these fits did not converge.

TABLE III. Initial condition of best fits (epoch of 152.444 days after 01/00/87).

Variable	Best	Uncertainty	Second Best
θ	2.881	.13	2.437
ϕ	0.679	.08	2.991
ψ	1.211	.27	0.426
$\dot{\theta}$	-1.710	.04	1.104
$\dot{\phi}$	0.009	.26	-2.374
$\dot{\psi}$	1.111	.13	-0.000
A/C	0.533	.05	0.529
B/C	0.782	.09	0.745
G	0.074	.03	0.101
H	13.851	.13	13.853
χ^2	0.144		0.206

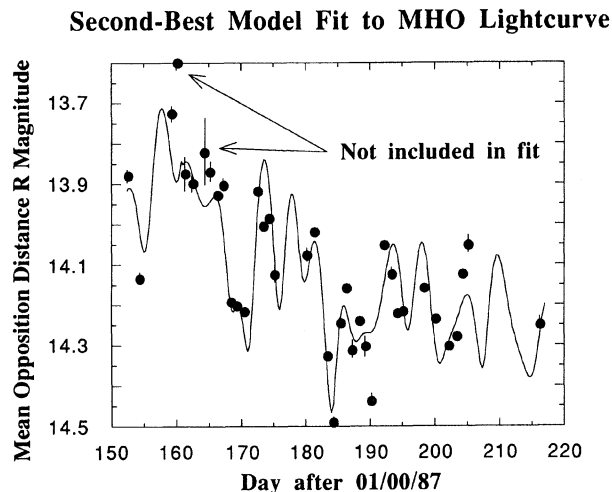


FIG. 12. Second-best model fit to MHO light curve.

e) Summary

In this section I first demonstrated that there was no simple period that could be adequately fit to the MHO light curve. For this, I used PDM analysis over a range of 2 hr to 30 days. Since Hyperion does not appear to be rotating in any periodic state, I proceeded to fit the dynamical model introduced in Sec. II to the light curve. I demonstrated the procedure necessary to convert the dynamical state variables to magnitudes which can be compared to the observed light curve. This involved transforming the state variables to an Earth-based frame and determining the projected area of an ellipsoid with those transformed variables. I then showed the proper procedure for fitting to the Hyperion light curve using numerical simulations. Counterintuitively, this involves first using only a subset of the light curve and then adding observations during the final fitting process. Finally, I fit the model to my light curve and presented the results. The next section will discuss these procedures and results.

IV. DISCUSSION

Voyager data of Hyperion's shape led Wisdom *et al.* (1984) to predict that Hyperion would be in a rotation state of chaotic tumbling. They first showed that Hyperion's phase space exhibits large scale chaos because of resonance overlap. A surface of section for Hyperion (Fig. 4) was calculated by integrating the equations of motion when the satellite was constrained to having its spin axis perpendicular to the orbital plane. This surface of section clearly shows the large chaotic zone surrounding the synchronous, 1:2, and 2:1 states. These states are attitude unstable and therefore inaccessible as Hyperion tidally evolves through phase space. Numerical simulations indicate that the probability of capture into any of the other resonance states is very small. The full equations of motion of the Hyperion spin-orbit coupling system were integrated by Wisdom *et al.* (1984) and they found all Lyapunov exponents to be nonzero, indicating that the system is chaotic.

Hyperion's rotation state has been investigated from ground-based and spacecraft observations. All previous observations of Hyperion were undersampled or had problems

with background gradient fitting and subtraction, thus making them inadequate for determining Hyperion's rotation state. Peale (1986), Wisdom *et al.* (1984), Wisdom and Peale (1984), and Peale and Wisdom (1984) warn of the possible ambiguities of traditional methods of folding back the light curve and performing least-squares analysis on data sampled less than about once every 1.5 days for a chaotically rotating Hyperion. Goguen *et al.* (1983) and Thomas and Veverka (1985) find best-fit periods using this technique. Both fits, however, produce results internally inconsistent with their datasets (see Paper I). Although there have been observations consistent with chaotic rotation, none of the previous observations have been able to definitively constrain the rotation state of Hyperion.

As described in Paper I, I observed Hyperion using the MHO 1.3 and 2.4 m telescopes with the MASCOT/MIS detector at the required sampling rate. My light curve contains 38 nightly means, an average of nine independent Hyperion observations per night, over an interval of 64 days. I found that Hyperion is essentially a constant brightness over a period of one night (6 hr) and that its color is $V - R = 0.41 \pm 0.02$. The light-curve amplitude, after correction to mean opposition magnitude, is ≈ 0.6 mag. This is consistent with the *Voyager*-derived shape.

Using PDM analysis, I demonstrated that no period from 1 hr to 30 days fits the light curve. Although a large part of the discussion in Paper I and Sec. III concentrated on fitting the H , G phase function to my light curve, the essential point is that the analysis is insensitive to the form of the phase correction. This was demonstrated by comparing the PDM plots with and without phase correction, which showed that the two plots are very similar (Paper I). Even the best period found from PDM analysis, however, does not fit the data well. This was shown statistically, as well as through inspection of the rotational phase plot in Paper I.

CCD photometry of Hyperion over an interval of 64 days shows no evidence of periodic modulation in the light curve. There are three possible explanations: (1) The motion is simply periodic but I have large, undetected errors in my light curve; (2) the motion is periodic in a complicated manner; or (3) the motion is chaotic.

The light curve is sound. The stability of Titan, the standard stars, and field stars in the same background gradient as Hyperion provides evidence that all aspects of the data acquisition and reduction are done consistently and correctly. Although it is possible that undetected error can inadvertently be introduced into any dataset, I have made certain that any error in my light curve is not large enough to invalidate the period-determination analysis, as detailed in Paper I.

There are no known dynamical perturbations that would stabilize the rotation state of Hyperion. The object which could have the largest effect on Hyperion, other than Saturn, is Titan. Even at closest approach, however, Titan's gravitational effect is only 3% that of Saturn. Tidal effects of Titan are another order of magnitude smaller than Saturn's. Integrated over the entire orbit, Titan's interaction would certainly be unable to affect Hyperion's rotation state enough to significantly alter the light curve.

No periodicities were found that adequately described my light curve. Is this conclusion equivalent to Hyperion being chaotic? Chaos has a very specific definition: chaotic motion is deterministic but unpredictable motion due to exponential divergence of nearby initial conditions. The equations of mo-

tion are known for the Hyperion spin-orbit coupling problem. Thus, the motion is deterministic: if a well-defined initial condition is given, the rotation state at any other time can, in principle, be calculated. Even infinitesimal uncertainties, however, limit this predictive ability. It is the exponential divergence of nearby initial conditions which gives chaotic systems their apparent random nature. While this work does not, and cannot, *prove* Hyperion is in a chaotic rotation state, it is very strong circumstantial evidence that Hyperion is tumbling chaotically. This is the only dataset from which this can be stated with conviction because of the problems with previous observations/analyses and because this is a high-quality, well-sampled light curve. *Voyager 2*, in addition to determining the size and shape of Hyperion, found the orientation of this satellite to be with its spin axis nearly parallel to the orbital plane (Thomas and Veverka 1985). This orientation would be difficult to reconcile with any regular rotation state.

Various modifications to the dynamical model presented in Sec. II were introduced in the last section to account for the observational details of the light curve. The time of the observations were corrected for light travel time. This allowed the true position of Hyperion in its orbit at any particular time to be calculated from its orbital elements. I then demonstrated the procedure necessary to calculate the relative magnitude of an observation based on its rotation state by transforming the spatial coordinates to a geocentric system and converting the projected area of the ellipsoid to a magnitude.

Numerical simulations allowed me to determine the best method of fitting the model to a light curve. Finding the initial conditions is a two step process. First, a well-sampled subset of the light curve is used to find the general area of phase space corresponding to the true initial conditions. The model then should be fit to the subset and the rest of the observations should be added singly, fitting each time for the light curve.

Phase space becomes increasingly complex as the number of observations increases. This suggests that a search of phase space by a well-sampled subset of the light curve should be used to determine an approximation of the initial condition. For most applications it is usually best to gather as much data as possible and then do whatever fitting is necessary. For a chaotic system this may not be the best strategy. Consider, for example, fitting the model to one observation: there are a number of initial conditions scattered throughout phase space that would fit the data, but there will be a greater number of nearby initial conditions which will quickly diverge from the dataset. As more observations are added, it is obvious that the number of initial conditions that approximate the data will decrease, but their immediate surroundings in phase space will get increasingly complex. This would not be the case for a dynamically regular system.

After the approximate initial condition is found, the light-curve subset can then be fit with some minimization routine to better define the initial condition. The next point in the light curve should then be added and the initial conditions for this new subset fit. This procedure continues until the model has been fit to the entire light curve. Such a technique has been used successfully for a simulated Hyperion dataset (Klavetter 1985, unpublished) and a simple chaotic system (Wisdom 1987; Chakrabarty 1988, unpublished). In contrast with the usual $1/\sqrt{N}$ decrease in the uncertainty of the initial condition expected from elementary statistics, these

studies found that when fitting to chaotic trajectories an exponential decrease in the uncertainties was found. Noting the definition of chaos, it makes sense that this should be so. As the number of observations increases, two rotation states that were initially close together and fit the first part of the light curve would begin to diverge and only one would fit the rest of the light curve well. My numerical simulations indicate that when a dataset spans an interval of time on the same order as the light curve, the initial conditions can be determined with high precision.

The best-fit light curve using this technique is shown in Fig. 11. One measure of the significance of the fit is to compare the internal uncertainties with the measured χ^2 , the sum of the observed minus the calculated magnitudes. For a good fit, the square root of χ^2 normalized by the number of observations would be approximately equal to the measured uncertainties. For the best-fit light curve shown in Fig. 11, $\sqrt{\chi^2/N} = 0.06$, where $N = 36$ is the number of observations. The measured uncertainties include a combination of the observational uncertainty, typically $\sigma_o \approx 0.02$, the uncertainty in Hyperion's shape, $\sigma_s \approx 0.04$, and the uncertainty in Hyperion's albedo variation, $\sigma_a \approx 0.01$ (the shape and albedo uncertainties will be discussed below). Thus, the total uncertainty is $\sigma_T \approx 0.05$, comparable to the model uncertainty of 0.06, such that the ratio of the two values is 1.2. Inspection of Fig. 11 confirms that the fit is not unreasonable. Given the uncertainties inherent in the present precision of Hyperion's shape and albedo, this may be the best fit possible.

My search of phase space and subsequent fitting determined the rotation state of Hyperion, including the two principal moment of inertia ratios. Due to the chaotic nature of the system, however, all dynamical information contained in the state variables is lost in approximately two Hyperion orbit periods (Wisdom *et al.* 1984). Thus, the rotation state would not be known now even if I had obtained a precise fit to the light curve with no errors in shape and albedo. This demonstrates the futility of attempting to combine all Hyperion measurements made over time intervals greater than approximately 40 days. The moment ratios, however, can provide information on Hyperion's internal structure.

Using the best-fit ellipsoid to *Voyager* data, Duxbury (as reported in Wisdom *et al.* 1984) found the following values for the principal semiaxes:

$$a = 190 \text{ km,}$$

$$b = 145 \text{ km,}$$

$$c = 114 \text{ km,}$$

with an uncertainty of 15 km. The moment ratios and their formal uncertainties are

$$A/C = 0.60 \pm 0.122,$$

$$B/C = 0.86 \pm 0.159.$$

These values are consistent with the best-model-fit values of $A/C = 0.54 \pm 0.05$ and $B/C = 0.79 \pm 0.09$. The uncertainties of the moment ratios are large for both the *Voyager*-derived values and the fitted values. However, the fitted values are consistent with those derived from the *Voyager* images, indicating that Hyperion is not grossly inhomogeneous if the fit is valid.

Although errors are listed in Table III, the simplex routine does not propagate any formal errors. After I had found the initial condition using the techniques described in the

last section, I numerically calculated the derivatives necessary to refit the entire light curve using nonlinear least-squares techniques. This was feasible since I had already found the best fit with the simplex algorithm. The least-squares result did not give me any more information about the rotation state. However, inversion of the covariance matrix yielded formal uncertainties based on the data, listed in Table III.

There are other effects to consider when using a fitting algorithm. Inspection of the solar phase plot (Fig. 3, Paper I) shows that data at solar phase angles $\alpha \geq 0.3^\circ$ are described adequately by the H, G phase function, within the uncertainties due to the aspect of Hyperion. The opposition surge, however, is not necessarily fit well with this phase function. This is why I did not include the observation nearest opposition in my model fitting. It is possible to separate the phase effect from the rotational effect by simultaneously fitting the dynamical model and the chosen phase function to the light curve. For the best model fit, the slope parameter $G = 0.074 \pm 0.03$ is consistent with the observationally fitted value of $G = 0.056 \pm 0.14$. Thus, the slope parameter is less than the expected value for C-type asteroids, approximately 0.15 (Bowell *et al.* 1987).

Thomas and Veverka (1985) report that any albedo variations are "mostly averaged out over the disk." This is confirmed by an inspection of Fig. 1, one of the highest resolution images obtained by *Voyager 2*. To quantify the variation in Hyperion's albedo, I measured the mean signal in a 10×10 box placed at five separated places on the disk of the Hyperion image shown in Fig. 1. The results are listed in Table IV. The mean varies by less than the standard deviation of about 3 ADUs. From this image, it appears as if albedo variations are indeed small when averaged over the disk. There is about a 1% mean variation, $\sigma_a \approx 0.01$.

The largest uncertainty in the model is Hyperion's shape. Figure 13 [Plate 60] is a *Voyager* image of Hyperion which presents a view not well approximated by an ellipsoid, and Thomas and Veverka (1985) note that Hyperion "cannot be described well by an ellipsoid." Thomas *et al.* (1986) plot the deviations of Hyperion's limb from a best-fit ellipse over 160° of arc. They find variations of up to $\pm 10\%$ for specific places along the limb with a mean deviation of approximately 3%–5%. Without a greater coverage of Hyperion's topography from spacecraft observations, it is impossible to rigorously assess the problems this will cause any model-fitting algorithm.

Numerical simulations indicate that model fitting can still be successful for reasonable errors in the ellipsoid's shape. Figure 14 is a plot of the error in the ellipsoid shape versus the residuals to the light curve. For this figure, a light curve was generated with a known initial condition and a Gaussian error of the specified amount was added to each observation. The model was then fit to the light curve using the known initial condition as a starting guess for the simplex algo-

Effect of Shape Error on Initial Condition

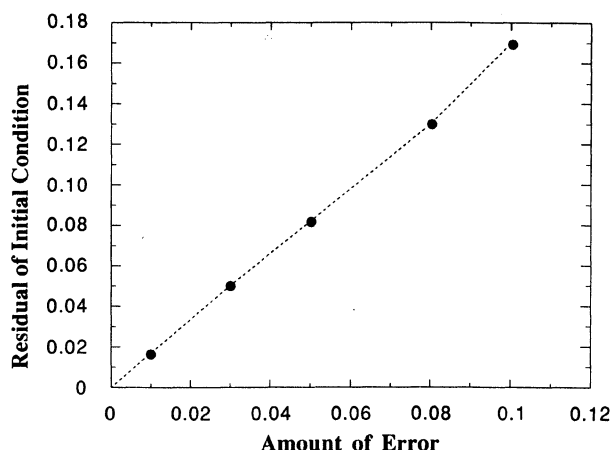


FIG. 14. Light curves were generated for one initial condition with varying amounts of Gaussian error added to each observation to simulate shape errors. The difference between the fitted initial condition and the true initial condition, calculated as the root of the sum of the normalized χ^2 , is plotted on the ordinate versus the amount of error. The dotted line connects the individual points.

riithm. The residuals were calculated by taking the square root of the sum of the square of the individual differences between the fitted initial conditions and the known initial conditions used to generate the light curve. There is a roughly linear relationship between the amount of error and the residuals. The fitted initial conditions remain relatively near the true value. Thus, if the approximate initial condition can be found, even shape errors as large as 8%–10% will still allow an accurate determination of the initial conditions to be made, but the results will be less precise.

Neglecting the small higher-order terms in the expansion of the potential, the motion of Hyperion is independent of the details of its shape. The equations of motion in this very good approximation depend on the principal moments of inertia, and not explicitly on the shape. The same motion would be observed for a homogeneous ellipsoid or a sphere whose mass distribution was such that both objects had the same values for the principal moments of inertia. The connection between shape and moments of inertia is that the moments are estimated from the shape for a body of homogeneous composition. The only parameter in the model that is explicitly dependent on the shape is the projected area of the ellipsoid, and thus the relative magnitude. Errors propagated to the relative magnitudes, however, will be less pronounced.

Deviations of the amount shown by Thomas *et al.* (1986) would typically affect the projected area, and therefore the relative magnitude, of Hyperion by $\leq 3\%$ – 4% . From Fig. 14, it is seen that this error in the initial condition is approximately 5%. This is the maximum precision possible with this model given perfect data and precise fitting.

Does my fitted light curve represent the best possible fit to the data? Only a rigorous search of phase space at better sampling can answer this question. However, the best model fit light curve is a fair fit to the data, as can be seen by inspection of Fig. 11 and the comparison of uncertainties noted above. For the second-best fit, the light curve uncertainty is

TABLE IV. Hyperion albedo variations.

Relative Location	Mean of 100 pixels	Standard Deviation
75, 57	40.02	4.00
58, 75	43.89	2.99
70, 63	40.12	3.05
64, 80	39.98	4.44
81, 64	40.88	3.61

0.08, almost a factor of 2 greater than the expected uncertainty. Due to the nature of fitting to chaotic motion, once the fit starts off in some slightly wrong direction in phase space, it can remain so far away as to never get back to the "correct" answer. This was seen in various numerical simulations I performed. In addition, inspection of the light curve and residuals show that it is not a good fit.

It is impossible, therefore, to state definitely that I have fit for the "true" initial condition. However, based on my numerical simulations I have marginally sampled phase space at the required sampling rate to find the correct initial condition. It is still possible that even with double the amount of sampling, the true initial condition would remain undetected. Furthermore, given the uncertainties in Hyperion's shape, it may be an impossibility to fit the model to the MHO light curve any better than I have done.

Based on my numerical simulations, however, it appears possible to do the fit. This fit has been performed and the results produced by following my procedure yield reasonable values for the moment ratios, consistent with Hyperion having a uniform density.

V. CONCLUSIONS

Observational (from Paper I):

- (1) Hyperion is not in any regular/periodic rotation state.
- (2) Hyperion exhibits a strong brightness variation with phase, including an opposition surge of approximately 0.3 mag at solar phase angles of less than about 0.3° . The numbers are imprecise because of the rotational effects.
- (3) Hyperion varies less than 0.01 mag over timescales of less than 6 hr.
- (4) The color of Hyperion is $V - R = 0.41 \pm 0.02$.

Dynamical:

- (1) To find the approximate initial condition, it is better to search phase space with a well-sampled subset of the light curve than the entire light curve. I do not know if this is a general result that could be related to all chaotic systems.
- (2) If the approximate initial condition could be found via the exhaustive search of phase space or some other method, a subset of the light curve should be fit, add the next observation, fit again, and repeat the process

for the entire light curve. There will be an exponential decrease in the uncertainty of the rotation state and the principal moments of inertia up to some limit due to the uncertainty of Hyperion's shape. This exponential decrease in the uncertainties of the initial conditions could be a general feature of chaotic systems.

- (3) Best-fit values of the Hyperion moment ratios are consistent with Hyperion being a body with a uniform mass distribution.

I thank David Jewitt for his financial and moral support. Jack Wisdom generously provided computer time and helpful discussions. I also thank the other members of my committee: James L. Elliot, Edward W. Dunham, and Richard G. French. Deepto Chakrabarty also provided many helpful discussions. Amanda Bosh helped with two of the figures, and Anita M. Killian read the manuscript and provided helpful suggestions. I also wish to thank the reviewer for careful reading and helpful suggestions. I extend a special thanks to John Swomley and Jennifer Roberts for taking care of Reudi while Athabasca and I were observing in Arizona and Chile.

APPENDIX A: DERIVATION OF THE TRANSFORMATION MATRIX

The transformation matrix A defined by $\mathbf{x} = A\mathbf{x}'$, where the primed coordinates are the body axes and the unprimed coordinates are the Saturnocentric axes, is a combination of the three simple rotations described in Sec. II. These rotations are actually transforming from the Saturnocentric axes to the body axes through the three Euler angles such that $A^{-1} = BCD$ where the three rotations defining the Euler angles are

$$D = \begin{bmatrix} \cos \theta & \sin \theta & 0 \\ -\sin \theta & \cos \theta & 0 \\ 0 & 0 & 1 \end{bmatrix},$$

$$C = \begin{bmatrix} 1 & 0 & 0 \\ 0 & \cos \varphi & \sin \varphi \\ 0 & -\sin \varphi & \cos \varphi \end{bmatrix},$$

$$B = \begin{bmatrix} \cos \psi & \sin \psi & 0 \\ -\sin \psi & \cos \psi & 0 \\ 0 & 0 & 1 \end{bmatrix},$$

as described in Sec. II. It should be noted that the Saturnocentric coordinate system is inertial and is defined by Hyperion's orbit at periapse. Performing the above rotations in this order produces

$$A^{-1} = \begin{bmatrix} \cos \theta \cos \psi - \sin \theta \cos \varphi \sin \psi & \sin \theta \cos \psi + \cos \theta \cos \varphi \sin \psi & \sin \varphi \sin \psi \\ -\cos \theta \sin \psi - \sin \theta \cos \varphi \cos \psi & -\sin \theta \sin \psi + \cos \theta \cos \varphi \cos \psi & \sin \varphi \cos \psi \\ \sin \theta \sin \varphi & -\cos \theta \sin \varphi & \cos \varphi \end{bmatrix}$$

such that A^{-1} is the inverse of A defined above. Since A^{-1} is a product of simple rotational matrices, $A^{-1} = A^T$ (Goldstein 1981). A is the transpose of the matrix above:

$$A = \begin{bmatrix} \cos \theta \cos \psi - \sin \theta \cos \varphi \sin \psi & -\cos \theta \sin \psi - \sin \theta \cos \varphi \cos \psi & \sin \theta \sin \varphi \\ \sin \theta \cos \psi + \cos \theta \cos \varphi \sin \psi & -\sin \theta \sin \psi + \cos \theta \cos \varphi \cos \psi & -\cos \theta \sin \varphi \\ \sin \varphi \sin \psi & \sin \varphi \cos \psi & \cos \varphi \end{bmatrix}.$$

The Wisdom coordinates are similar to the Euler coordinates except the third rotation is

$$B^W = \begin{bmatrix} \cos \psi & 0 & -\sin \psi \\ 0 & 1 & 0 \\ \sin \psi & 0 & \cos \psi \end{bmatrix},$$

where the superscript denotes that this is a rotation matrix for the Wisdom coordinates. For this set of rotations, the transformation matrix is

$$A^W = \begin{bmatrix} \cos \theta \cos \psi - \sin \theta \cos \varphi \sin \psi & -\sin \theta \cos \varphi & \cos \theta \sin \psi + \sin \theta \sin \varphi \cos \psi \\ \sin \theta \cos \psi + \cos \theta \sin \varphi \sin \psi & \cos \theta \cos \varphi & \sin \theta \sin \psi - \cos \theta \sin \varphi \cos \psi \\ -\cos \varphi \sin \psi & \sin \varphi & \cos \varphi \cos \psi \end{bmatrix},$$

where the angles are now in Wisdom coordinates.

If the orientation of the satellite with respect to the planet is required, the above needs to be modified. $\theta - f$ is angle between the ellipsoid's long axis and the satellite to planet line. This is not necessary for any of the transformations discussed in this work.

These transformation matrices will be used in the calculations of the direction cosines, the calculation of projected area, and in converting coordinate systems which will be described in following appendices.

APPENDIX B: DERIVATION OF ANGULAR VELOCITY IN EULER COORDINATES

In Sec. II, the angles of the Euler coordinate system were defined. When θ , φ , and ψ change with time, the angular velocities associated with these angles will be about the axes shown in Fig. 3 (Sec. II) such that $\omega = \dot{\theta}\hat{z} + \dot{\varphi}\hat{x}' + \dot{\psi}\hat{c}$. This is easily seen by setting any two of the angular velocities to zero and noting about which axis the third is rotating. The derivation of the equations of motion in Sec. II and Appendix D requires $\omega = \omega_a\hat{a} + \omega_b\hat{b} + \omega_c\hat{c}$. The transformation between the dynamical state variables and the components of ω will be derived in this appendix.

The first intermediate axes are

$$\hat{x}' = \hat{a} \cos \psi - \hat{b} \sin \psi,$$

$$\hat{y}' = \hat{a} \sin \psi + \hat{b} \cos \psi,$$

and

$$\hat{z} = \hat{c} \cos \varphi + \hat{y}' \sin \varphi.$$

Substituting for \hat{y}' :

$$\hat{z} = \hat{a} \sin \varphi \sin \psi + \hat{b} \sin \varphi \cos \psi + \hat{c} \cos \varphi.$$

Now everything can be described in terms of the body axes. Final substitution produces

$$\omega_a = \dot{\theta} \sin \varphi \sin \psi + \dot{\varphi} \cos \psi,$$

$$\omega_b = \dot{\theta} \sin \varphi \cos \psi - \dot{\varphi} \sin \psi,$$

$$\omega_c = \dot{\theta} \cos \varphi + \dot{\psi}$$

as in Sec. II. The derivation in Wisdom coordinates proceeds along similar lines and the angular velocities in this case are

$$\omega_a^W = -\dot{\theta} \cos \varphi \sin \psi + \dot{\varphi} \cos \psi$$

$$\omega_b^W = \dot{\theta} \sin \varphi + \dot{\psi}$$

$$\omega_c^W = \dot{\theta} \cos \varphi \cos \psi + \dot{\varphi} \sin \psi.$$

APPENDIX C: CALCULATION OF DIRECTION COSINES

The direction cosines are needed to specify the equations of motion, as described in Sec. II and Appendix D. Direction cosines are defined as (see Fig. 2)

$$\alpha \equiv \hat{x} \cdot \hat{a},$$

$$\beta \equiv \hat{x} \cdot \hat{b},$$

$$\gamma \equiv \hat{x} \cdot \hat{c},$$

where \hat{x} is the planet to satellite unit vector, as defined in Sec. III, and a , b , and c are the body axes. As in Sec. III, let the body axes be noted by a primed coordinate system such that

$$\alpha = \hat{x} \cdot \hat{x}',$$

$$\beta = \hat{x} \cdot \hat{y}',$$

$$\gamma = \hat{x} \cdot \hat{z}.$$

As noted in Sec. III, $\mathbf{x} = A\mathbf{x}'$ so the direction cosines are merely the matrix elements

$$\alpha = A_{11},$$

$$\beta = A_{12},$$

$$\gamma = A_{13}.$$

Referring to the transformation matrix in Appendix A, the direction cosines are

$$\alpha = \cos \theta \cos \psi - \sin \theta \cos \varphi \sin \psi,$$

$$\beta = -\cos \theta \sin \psi - \sin \theta \cos \varphi \cos \psi,$$

$$\gamma = \sin \theta \sin \varphi.$$

Similarly for the direction cosines in Wisdom coordinates

$$\alpha = A_{11}^W,$$

$$\beta = A_{12}^W,$$

$$\gamma = A_{13}^W,$$

where the superscript signifies the transformation matrix is in the Wisdom coordinates. Again, referring to Appendix A, the direction cosines in these coordinates are

$$\alpha^W = \cos \theta \cos \psi - \sin \theta \sin \varphi \sin \psi,$$

$$\beta^W = -\sin \theta \cos \varphi,$$

$$\gamma^W = \cos \theta \sin \psi + \sin \theta \sin \varphi \cos \psi,$$

where the rotation angles are now understood to be the Wisdom coordinates, as defined in Sec. II and Appendix A.

APPENDIX D: EQUATIONS OF MOTION

In Sec. II, I outlined the derivation of the equations of motion in Euler coordinates. In this appendix, the details of this derivation will be given as well as the full equations of motion.

As shown in Sec. II, the Euler equations for the spin-orbit coupling system of the Hyperion model considered are

$$\begin{aligned} A \frac{d\omega_a}{dt} - \omega_b \omega_c (B - C) &= -\frac{3}{r^3} \beta \gamma (B - C), \\ B \frac{d\omega_b}{dt} - \omega_c \omega_a (C - A) &= -\frac{3}{r^3} \gamma \alpha (C - A), \\ C \frac{d\omega_c}{dt} - \omega_a \omega_b (A - B) &= -\frac{3}{r^3} \alpha \beta (A - B). \end{aligned} \quad (D1)$$

The direction cosines defined in Appendix C are

$$\begin{aligned}\alpha &= \cos \theta \cos \psi - \sin \theta \cos \varphi \sin \psi, \\ \beta &= -\cos \theta \sin \psi - \sin \theta \cos \varphi \cos \psi, \\ \gamma &= \sin \theta \sin \varphi\end{aligned}\quad (\text{D2})$$

and the angular velocities about the body axes in Euler coordinates as derived in Appendix B are

$$\begin{aligned}\omega_a &= \dot{\theta} \sin \varphi \sin \psi + \dot{\varphi} \cos \psi, \\ \omega_b &= \dot{\theta} \sin \varphi \cos \psi - \dot{\varphi} \sin \psi, \\ \omega_c &= \dot{\theta} \cos \varphi + \dot{\psi}\end{aligned}\quad (\text{D3})$$

as given in Sec. II.

Differentiating Eq. (D3) with respect to time yields

$$\begin{aligned}\dot{\omega}_a &= \ddot{\theta} \sin \varphi \sin \psi + \dot{\theta} \dot{\varphi} \cos \varphi \sin \psi + \dot{\theta} \dot{\psi} \sin \varphi \cos \psi \\ &\quad + \ddot{\varphi} \cos \psi - \dot{\varphi} \dot{\psi} \sin \psi, \\ \dot{\omega}_b &= \ddot{\theta} \sin \varphi \cos \psi + \dot{\theta} \dot{\varphi} \cos \varphi \cos \psi - \dot{\theta} \dot{\psi} \sin \varphi \sin \psi \\ &\quad - \ddot{\varphi} \sin \psi - \dot{\varphi} \dot{\psi} \cos \psi, \\ \dot{\omega}_c &= \ddot{\theta} \cos \varphi - \dot{\theta} \dot{\varphi} \sin \varphi + \ddot{\psi}.\end{aligned}$$

Then substituting the above into Eq. (D1):

$$\begin{aligned}\ddot{\theta} \sin \varphi \sin \psi + \ddot{\varphi} \cos \psi &= k_1, \\ \ddot{\theta} \sin \varphi \cos \psi - \ddot{\varphi} \sin \psi &= k_2, \\ \ddot{\theta} \cos \varphi + \ddot{\psi} &= k_3,\end{aligned}$$

where

$$\begin{aligned}k_1 &\equiv \left(\omega_b \omega_c - \frac{3}{r^3} \beta \gamma \right) \frac{B - C}{A} - \dot{\theta} \dot{\varphi} \cos \varphi \sin \psi \\ &\quad - \dot{\theta} \dot{\psi} \sin \varphi \cos \psi + \dot{\varphi} \dot{\psi} \sin \psi, \\ k_2 &\equiv \left(\omega_c \omega_a - \frac{3}{r^3} \gamma \alpha \right) \frac{C - A}{B} - \dot{\theta} \dot{\varphi} \cos \varphi \cos \psi \\ &\quad + \dot{\theta} \dot{\psi} \sin \varphi \sin \psi + \dot{\varphi} \dot{\psi} \cos \psi, \\ k_3 &\equiv \left(\omega_a \omega_b - \frac{3}{r^2} \alpha \beta \right) \frac{A - B}{C} + \dot{\theta} \dot{\varphi} \sin \varphi.\end{aligned}$$

These are the equations of motion for the spin-orbit coupling model defined in Sec. II. If a rotation state is known, only the three angular accelerations are unknown and these equations can be solved to give

$$\begin{aligned}\ddot{\theta} &= \frac{k_1 \sin \psi + k_2 \cos \psi}{\sin \varphi}, \\ \ddot{\varphi} &= k_1 \cos \psi - k_2 \sin \psi, \\ \ddot{\psi} &= k_3 - \ddot{\theta} \cos \varphi.\end{aligned}$$

In this form, the singularity of these equations mentioned in Sec. II is obvious. Whenever $\sin \varphi = 0$, these solutions are not defined. Of course a solution still exists, it is just impossible to express it in these coordinates. This is why an alternate set, the Wisdom coordinates, were also defined in Sec. II. The equations of motion in Wisdom coordinates are derived in exactly the same manner and the solutions are analogous to those above. The transformation from the Euler coordinate system to the Wisdom coordinate system is derived in Appendix F.

APPENDIX E: DETERMINATION OF HYPERION'S POSITION IN ITS ORBIT

As explained in Sec. III, it is necessary to know the position of Hyperion in its orbit. One of the state variables defining the initial condition is the true anomaly, related to the time of the observation. Utilizing the knowledge of Hyperion's

orbit from the *Explanatory Supplement to the Astronomical Ephemeris and the American Ephemeris and Nautical Almanac*, it is possible to calculate accurately the position of Hyperion in its orbit based on the time of the observation.

The mean anomaly l is found from the following relation

$$\begin{aligned}l &= 176^\circ.293 + n(\text{JD} - 2415020.0) \\ &\quad + 9^\circ.092 \sin \sigma + 0^\circ.211 \sin(x + \sigma) \\ &\quad + 0^\circ.092 \sin(x - \sigma) - 0^\circ.077 \sin x,\end{aligned}$$

where JD is the Julian Date, n is the tropical mean daily motion, $n = 16^\circ.9199896$, and the two periodic terms are defined as

$$\begin{aligned}\sigma &= 93^\circ.13 + 0^\circ.562039(\text{JD} - 2415020.0), \\ x &= 148^\circ.72 - 19^\circ.184t,\end{aligned}$$

where t is the time measured in tropical years from 1900.0. The long-period variable x is called $\tilde{\omega}$ in the *Explanatory Supplement* but I chose to use x to avoid confusion between this variable and the longitude of perihelion, $\tilde{\omega} \equiv \omega + \Omega$. The longitude of perihelion (called Π in the *Explanatory Supplement*) is given by

$$\begin{aligned}\tilde{\omega} &= 70^\circ.05 - 18^\circ.6562t - 13^\circ.67 \sin x \\ &\quad + 0^\circ.93 \sin 2x - 0^\circ.47 \sin \sigma.\end{aligned}$$

From the definitions of mean longitude, the mean anomaly is $M = l - \tilde{\omega}$. The mean anomaly specifies the position of Hyperion in its orbit, but the variable used in the analysis (see Sec. III) is the true anomaly. The true anomaly f can be found if the eccentric anomaly E is known. The eccentric anomaly can be found from solving Kepler's equation. For this, the eccentricity must also be known and is calculated using

$$\begin{aligned}e &= 0^\circ.10419 + 0^\circ.02414 \cos x \\ &\quad - 0^\circ.00401 \cos \sigma - 0^\circ.00183 \cos 2x.\end{aligned}$$

Solving Kepler's equation is an iterative process. I used the form

$$E_{k+1} = E_k + \frac{M - M_k}{1 - e \cos E_k},$$

$$M_k = E_k - e \sin E_k,$$

with an initial choice of the eccentric anomaly as

$$E_0 = M + \frac{e \sin M}{1 - \sin(M + e) + \sin M}.$$

Finally, to convert the eccentric anomaly to the true anomaly,

$$\tan \frac{f}{2} = \sqrt{\frac{1+e}{1-e}} \tan \frac{E}{2}.$$

This identity has the advantage that $f/2$ and $E/2$ are always in the same quadrant.

If desired, Hyperion's other orbital elements can be calculated in a similar manner. The goal of this appendix, however, is to show how the light-corrected time of an observation can be converted to a true anomaly corresponding to Hyperion's position in its orbit. As a check to this procedure, I compared the calculated values of the orbital elements to the tabulated values in the 1987 *Astronomical Almanac*. The calculated values were in general agreement with linear interpolated values from the tables. I used the calculated values because they are more accurate.

APPENDIX F: PROJECTED AREA OF AN ELLIPSOID

It is necessary to know the projected area of an ellipsoid to compare the model with my light curve. The equations of motion for an ellipsoid in the Hyperion-Saturn system were introduced in Sec. II and developed in Appendix D. These equations determine the dynamics of the system at all times for a given set of initial conditions or rotation state. The dynamics must then be converted to the observable magnitude for comparison to my data. If the area is known, the relative magnitude is $m = -2.5 \log A$ as shown in Sec. III. Thus, if the projected area of an ellipsoid can be derived from the state variables, the relative magnitude can be calculated and compared with the light curve.

The method of finding the projected area will be to convert the equation of an ellipsoid in the body axes

$$1 = \frac{x'^2}{a^2} + \frac{y'^2}{b^2} + \frac{z'^2}{c^2}$$

to the appropriate equation in the Saturnocentric axes and

$$\begin{aligned} A &\equiv \frac{\cos^2 \theta \cos^2 \psi + \sin^2 \theta \cos^2 \varphi \sin^2 \psi - 2 \cos \theta \sin \theta \cos \varphi \cos \psi \sin \psi}{a^2} \\ &\quad + \frac{\cos^2 \theta \sin^2 \psi + \sin^2 \theta \cos^2 \varphi \cos^2 \psi + 2 \cos \theta \sin \theta \cos \varphi \cos \psi \sin \psi}{b^2} + \frac{\sin^2 \theta \sin^2 \varphi}{c^2}, \\ B &\equiv \frac{\cos \theta \sin \theta \cos^2 \psi - \sin^2 \theta \cos \varphi \cos \psi \sin \psi - \cos^2 \theta \cos \varphi \cos \psi \sin \psi - \cos \theta \sin \theta \cos^2 \varphi \sin^2 \psi}{a^2} \\ &\quad + \frac{\cos \theta \sin \theta \sin^2 \psi + \sin^2 \theta \cos \varphi \cos \psi \sin \psi - \cos \theta \sin \theta \cos^2 \varphi \cos^2 \psi}{b^2} + \frac{-\cos \theta \sin \theta \sin^2 \varphi}{c^2}, \\ C &\equiv \frac{\cos \theta \sin \varphi \cos \psi \sin \psi - \sin \theta \cos \varphi \sin \varphi \sin^2 \psi}{a^2} \\ &\quad + \frac{-\cos \theta \sin \varphi \cos \psi \sin \psi - \sin \theta \cos \varphi \sin \varphi \cos^2 \psi}{b^2} + \frac{\sin \theta \cos \varphi \sin \varphi}{c^2}, \\ D &\equiv \frac{\sin^2 \theta \cos^2 \psi + \cos^2 \theta \cos^2 \varphi \sin^2 \psi + 2 \cos \theta \sin \theta \cos \varphi \cos \psi \sin \psi}{a^2} \\ &\quad + \frac{\sin^2 \theta \sin^2 \psi + \cos^2 \theta \cos^2 \varphi \cos^2 \psi - 2 \cos \theta \sin \theta \cos \varphi \cos \psi \sin \psi}{b^2} + \frac{\cos^2 \theta \sin^2 \varphi}{c^2}, \\ E &\equiv \frac{\sin^2 \varphi \sin^2 \psi}{a^2} + \frac{\sin^2 \varphi \cos^2 \psi}{b^2} + \frac{\cos^2 \varphi}{c^2}, \\ F &\equiv \frac{\sin \theta \sin \varphi \cos \psi \sin \psi + \cos \theta \cos \varphi \sin \varphi \sin^2 \psi}{a^2} \\ &\quad + \frac{-\sin \theta \sin \varphi \cos \psi \sin \psi + \cos \theta \cos \varphi \sin \varphi \sin^2 \psi}{b^2} + \frac{-\cos \theta \cos \varphi \sin \varphi}{c^2}. \end{aligned}$$

Differentiating this equation with respect to x will give an equation for the projection on the y - z plane, which is the plane perpendicular to the planet satellite radius vector. Differentiating with respect to x yields

$$0 = 2Ax + 2By + 2Cz$$

$$\Rightarrow x = -(By + Cz)/A.$$

This can be substituted back into the original equation to obtain the relation

$$1 = Gy^2 + 2Jyz + Hz^2,$$

where

then to compute the area of the resulting projection. Using the transformation matrix derived in Appendix A, this equation can be expressed in terms of the Saturnocentric axes. Using $\mathbf{x}' = \mathbf{A}^T \mathbf{x}$, in which the transformation matrix is defined in Appendix A, the body axes can be expressed as

$$\begin{aligned} x' &= (\cos \theta \cos \psi - \sin \theta \cos \varphi \sin \psi)x + (\sin \theta \cos \psi \\ &\quad + \cos \theta \cos \varphi \sin \psi)y + (\sin \varphi \sin \psi)z, \\ y' &= (-\cos \theta \sin \psi - \sin \theta \cos \varphi \cos \psi)x - (\sin \theta \sin \psi \\ &\quad + \cos \theta \cos \varphi \cos \psi)y + (\sin \varphi \cos \psi)z, \\ z' &= (\sin \theta \sin \varphi)x - (\cos \theta \sin \varphi)y + (\cos \varphi)z. \end{aligned}$$

Squaring these equations and substituting it into the equation of the ellipsoid produces an equation of the form

$$\begin{aligned} 1 &= Ax^2 + 2Bxy + 2Cxz \\ &\quad + Dy^2 + Ez^2 + 2Fyz, \end{aligned}$$

where

$$\begin{aligned} G &\equiv D - (B^2/A), \\ H &\equiv E - (C^2/A), \\ J &\equiv F - (BC/A), \end{aligned}$$

which is the equation for the projected curve of the ellipsoid as viewed from Saturn. This is also an alternate form for the equation of an ellipse if $4(J^2 - GH) < 0$ (Thomas and Finney 1980). This condition was checked in the programs I wrote to calculate the projected area, and found to be true. Thus, the projected area of an ellipsoid is an ellipse.

The angle of rotation of this ellipse is

$$\delta = \frac{1}{2} \tan^{-1} \left(\frac{2J}{G-H} \right),$$

which can be derived by expressing the equation of the ellipse in polar coordinates and finding the angle corresponding to maximum distance from the center. For polar coordinates

$$\tan \delta = z/y,$$

$$r^2 = y^2 + z^2,$$

the above equation for an ellipse becomes

$$r^2 = \frac{1 + \tan^2 \delta}{G + H \tan^2 \delta + 2J \tan \delta}.$$

Differentiating this with respect to δ and setting it equal to zero to maximize r yields the solution above.

The area of an ellipse is $A = \pi ab$ where a and b are the semimajor and semiminor axes. In this case,

$$A = \pi r(\delta) r[\delta + (\pi/2)],$$

where r is defined above. Since r is a function of the original state variables, the projected area can now be calculated with a knowledge of the dynamics.

As outlined in Sec. III, two additional rotations must be invoked to calculate the projected area as seen from Earth. The above derivation finds the relationship between the dynamical state variables and the projected area as seen from Saturn. The correction to a geocentric system is minor. Instead of using the transformation matrix defined in Appendix A, the two additional rotations must be included as

$$A'^T = BCDEF = A'^T EF,$$

where

$$E = \begin{bmatrix} \cos \xi & \sin \xi & 0 \\ -\sin \xi & \cos \xi & 0 \\ 0 & 0 & 1 \end{bmatrix},$$

$$F = \begin{bmatrix} \cos B & 0 & -\sin B \\ 0 & 1 & 0 \\ \sin B & 0 & \cos B \end{bmatrix}.$$

As defined in Sec. III, the angle ξ is the true anomaly plus the projection of the angle between the vector pointing to Earth and the vector pointing to periape on the ecliptic. The angle B is the declination of the Earth as seen from Saturn or Hyperion.

The derivation of the projected area as seen from Earth then proceeds in exactly the same manner to produce equations of the same form as above, differing only in how G , H , and J are defined. Thus, in deriving the equation of the projected area of Hyperion as seen from Saturn, I also derived the projected area of Hyperion as seen from Earth.

APPENDIX G: CONVERSION OF COORDINATE SYSTEMS

The equations of motion have a singularity when $\sin \varphi = 0$, in Euler coordinates (see Appendix D). Since these equations must be solved for a tumbling ellipsoid, it is inevitable that this condition will be approached and another set of coordinates must be used. The other set of coordinates, introduced by Wisdom *et al.* (1984), are defined in Sec. III and Appendix A. This appendix will detail the procedures used to convert from one set of coordinates to the other.

Since both the Euler angles and Wisdom angles are describing the same position of the ellipsoid in space, it follows that $A = A^W$. These matrices are given in Appendix A. As an example, if the Euler angles are known, equating the first and last elements in the bottom rows of the matrices produces the two relations

$$-\cos \varphi^W \sin \psi^W = \sin \varphi \sin \psi,$$

$$\cos \varphi^W \cos \psi^W = \cos \varphi,$$

so that

$$\tan \psi^W = \frac{\sin \varphi \sin \psi}{\cos \varphi}.$$

There is no ambiguity as to what quadrant the tangent belongs since the sign of the numerator and the denominator are both known. For this appendix, the Wisdom coordinates have a superscript "W" and the Euler coordinates do not. In a similar manner,

$$\tan \varphi^W = \frac{\sin \varphi \cos \psi}{(\cos \varphi / \cos \psi^W)}$$

$$\tan \theta^W = \frac{\cos \theta \sin \psi + \sin \theta \cos \varphi \cos \psi}{-\sin \theta \sin \psi + \cos \theta \cos \varphi \cos \psi},$$

for the other two angles.

The conversion of the velocity components is done in a similar manner. Since the velocity vector is independent of the coordinate system representation, $\omega = \omega^W$. The components of these vectors are given in Appendix B. Again, assume the Euler coordinates are known. Then, solving for the Wisdom coordinates gives

$$\dot{\theta}^W = \frac{c_3 \cos \psi - c_1 \sin \psi}{\cos \varphi},$$

$$\dot{\varphi}^W = c_3 \sin \psi + c_1 \cos \psi,$$

$$\dot{\psi}^W = c_2 - \dot{\theta}^W \sin \varphi^W,$$

where

$$c_1 = \dot{\theta} \sin \varphi \sin \psi + \dot{\varphi} \cos \psi,$$

$$c_2 = \dot{\theta} \sin \varphi \cos \psi - \dot{\varphi} \sin \psi,$$

$$c_3 = \dot{\theta} \cos \varphi + \dot{\psi}.$$

The procedure to convert Wisdom coordinates to Euler coordinates is analogous and gives similar results.

REFERENCES

- Andersson, L. E. (1974). "A Photometric Study of Pluto and Satellites of the Outer Planets," Ph.D. thesis, Indiana University, Bloomington.
- Binzel, R., Green, J., and Opal, C. (1986). *Nature* **320**, 511.
- Bowell, E., Harris, A., and Lumme, K. (1987). *Icarus* (submitted).
- Chakrabarty, D. (1988). *Determination of Initial Conditions for Chaotic Systems: Numerical Studies of the Standard Mapping* (unpublished).
- Chapman, C. R., and McKinnon, W. B. (1986). In *Satellites*, edited by J. A. Burns and M. S. Matthews (University of Arizona, Tucson), pp. 492–580.
- Chirikov, B. V. (1979). *Phys. Rep.* **52**, 263.
- Clark, R. N., Brown, R. H., Owensby, P. D., and Steele, A. (1984). *Icarus* **58**, 265.
- Conner, S. (1984). "Photometry of Hyperion," M.S. thesis, Massachusetts Institute of Technology, Cambridge.

- Cruikshank, D. P. (1979). *Rev. Geophys. Space Phys.* **17**, 165.
- Cruikshank, D. P., Bell, J. F., Gaffey, M. J., Brown, R. H., Howell, R., Beerman, C., and Rognstad, M. (1983). *Icarus* **53**, 90.
- Cruikshank, D. P., and Brown, R. H. (1982). *Icarus* **50**, 82.
- Degewij, J., Andersson, L. E., and Zellner, B. (1980). *Icarus* **44**, 520.
- Farinella, P., Milani, A., Nobili, A., Paolicchi, P., and Zappalà, V. (1983). *Icarus* **54**, 353.
- Franklin, F. A., and Cook, A. F. (1974). *Icarus* **23**, 355.
- Goguen, J., Cruikshank, D. P., Hammel, H., and Hartmann, W. K. (1983). *Bull. Am. Astron. Soc.* **15**, 854.
- Goldreich, P., and Peale, S. (1966). *Astron. J.* **71**, 425.
- Goldstein, H. (1981). *Classical Mechanics* (Addison-Wesley, Reading).
- Harris, D. L. (1961). In *Planets and Satellites*, edited by G. Kuiper and B. Middlehurst (University of Chicago, Chicago), pp. 272–342.
- Hénon, M., and Heiles, C. (1964). *Astron. J.* **69**, 73.
- Klavetter, J. J. (1985). "Observational Evidence of Hyperion's Chaotic Tumbling: Determination of Initial Conditions" (unpublished).
- Klavetter, J. J. (1989). *Astron. J.* **97**, 570 (Paper I).
- Peale, S. (1986). In *Satellites*, edited by J. A. Burns and M. S. Matthews (University of Arizona, Tucson), pp. 159–223.
- Peale, S., and Wisdom, J. (1984). *Bull. Am. Astron. Soc.* **16**, 686.
- Press, W. H., Flannery, B. P., Teukolsky, S. A., and Vetterling, W. T. (1986). *Numerical Recipes* (Cambridge University, Cambridge).
- Smith, B. A., Soderblom, L., Batson, R., Bridges, P., Inge, J., Masursky, H., Shoemaker, E., Beebe, R., Boyce, J., Briggs, G., Bunker, A., Collins, S. A., Hansen, C. J., Johnson, T. V., Mitchell, J. L., Terrile, R. J., Cook, A. F., Cuzzi, J., Pollack, J. P., Danielson, G. E., Ingersoll, A. P., Strom, M. E., Suomi, V. E. (1982). *Science* **215**, 504.
- Stellingwerf, R. (1978). *Astrophys. J.* **224**, 953.
- Tholen, D. J., and Zellner, B. (1983). *Icarus* **53**, 341.
- Thomas G. B., and Finney, R. L. (1980). *Calculus and Analytic Geometry* (Addison-Wesley, Reading).
- Thomas, P., and Veverka, J. (1985). *Icarus* **64**, 414.
- Thomas, P., Veverka, J., and Dermott, S. (1986). In *Satellites*, edited by J. A. Burns and M. S. Matthews (University of Arizona, Tucson), pp. 802–835.
- Thomas P., Veverka, J., Morrison, D., Davies, M., and Johnson, T. V. (1983). *J. Geophys. Res.* **88**, 8743.
- Thomas, P., Veverka, J., Wenkert, D., Danielson, G., and Davies, M. (1984). *Nature* **307**, 716.
- Wisdom, J. (1983). *Icarus* **56**, 51.
- Wisdom, J. (1987). *Icarus* **72**, 241.
- Wisdom, J., and Peale, S. (1984). *Bull. Am. Astron. Soc.* **16**, 707.
- Wisdom, J., Peale, S., and Mignard, F. (1984). *Icarus* **58**, 137.
- Woltjer, J. (1928). *Ann. Sterrewacht Leiden* **16**, 64.

PLATE 59

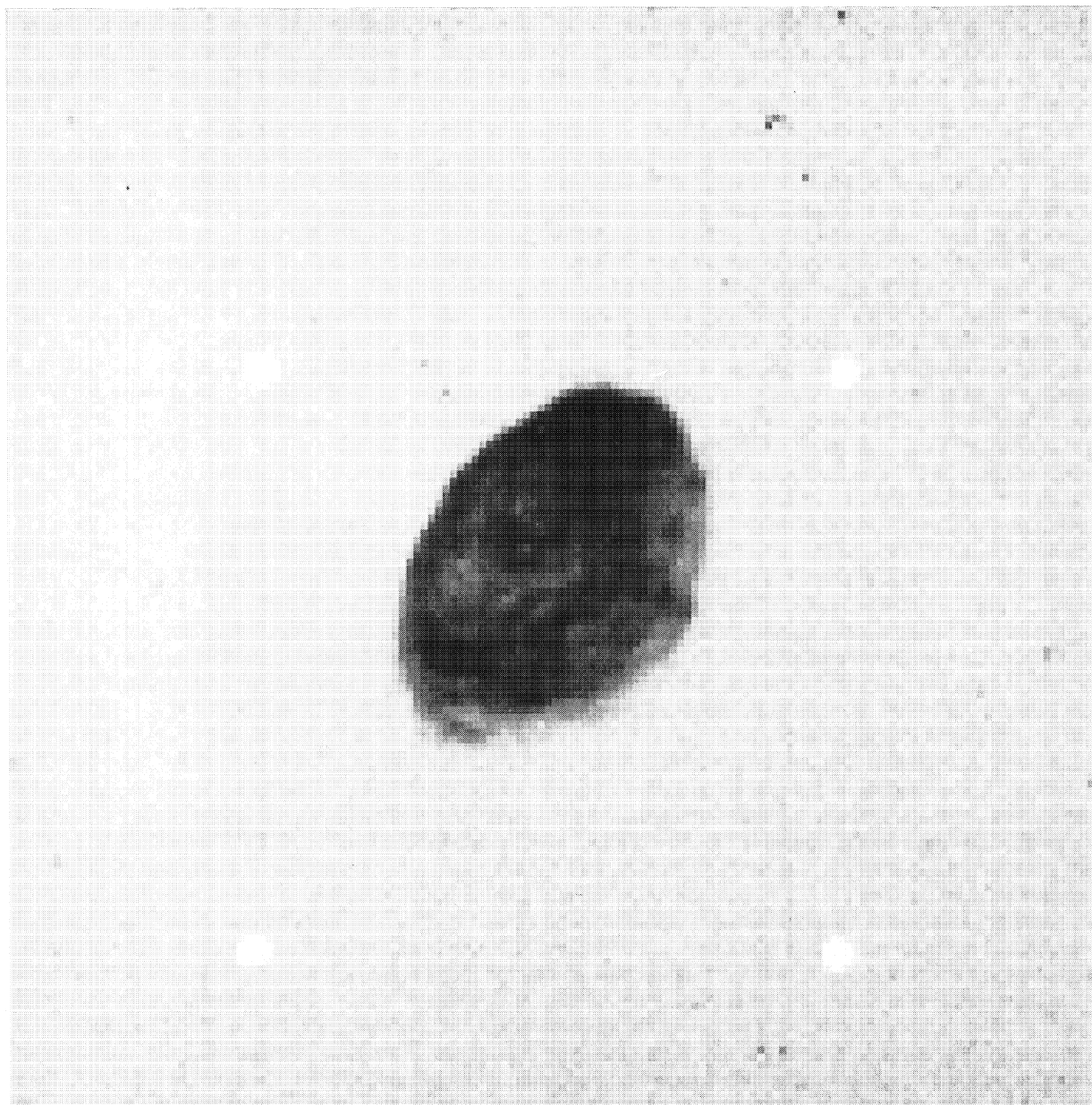


FIG. 1. One of the highest-resolution *Voyager* images of Hyperion. The terminator is to the right in this picture. Note that the outline is closely approximated by an ellipse. Even though this is a high-resolution image of Hyperion, surface features are difficult to distinguish. The albedo is approximately constant between different sections of the surface.

James Jay Klavetter (see page 1855)

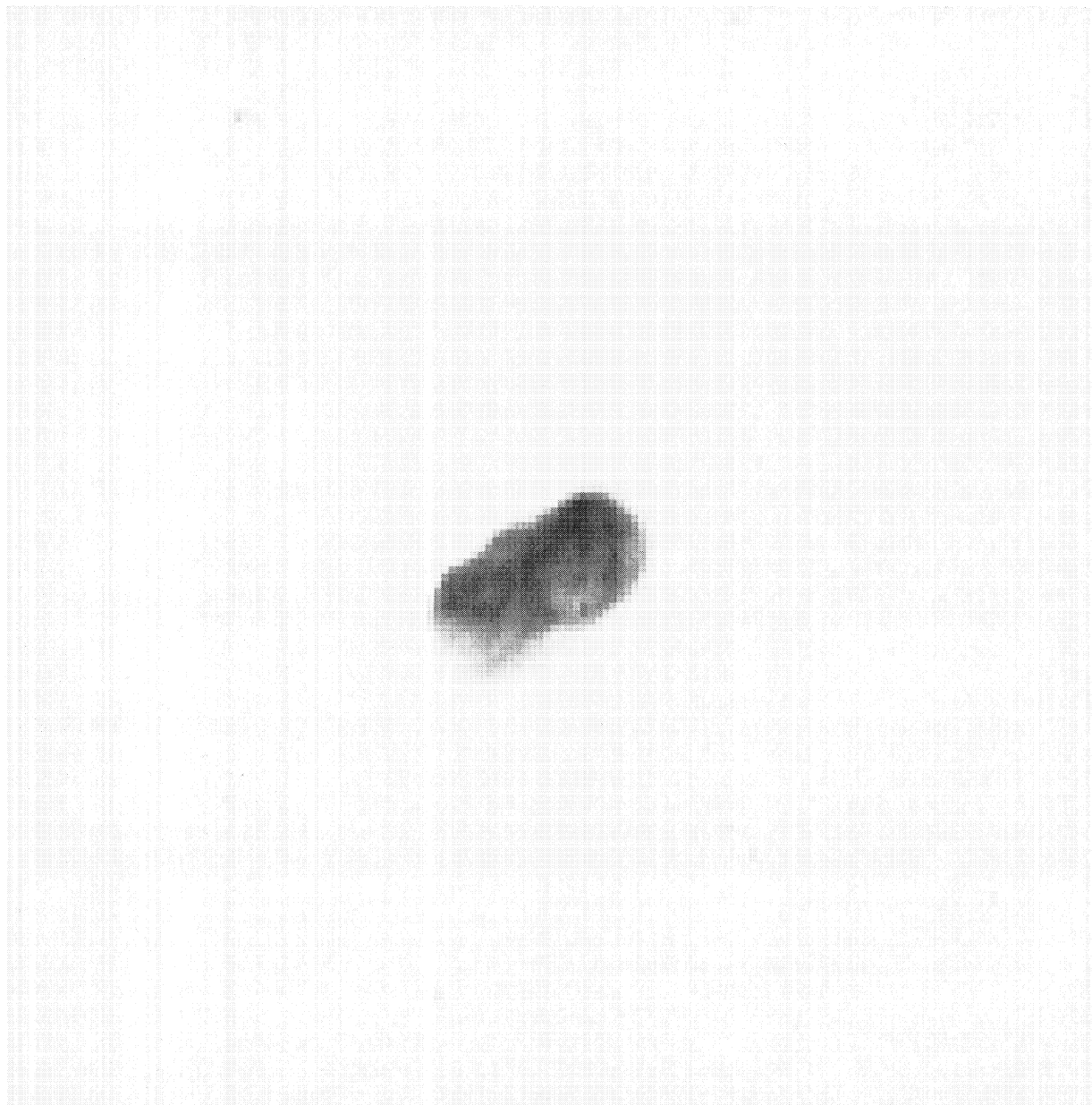


FIG. 13. Another high-resolution *Voyager* image (see Fig. 1). This one, however, does not appear to approximate an ellipse in cross section.

James Jay Klavetter (see page 1868)